

Die approbierte Originalversion dieser Diplom-/Masterarbeit ist an der Hauptbibliothek der Technischen Universität Wien aufgestellt (<http://www.ub.tuwien.ac.at>).

The approved original version of this diploma or master thesis is available at the main library of the Vienna University of Technology (<http://www.ub.tuwien.ac.at/englweb/>).



TECHNISCHE
UNIVERSITÄT
WIEN
Vienna University of Technology

DIPLOMARBEIT

TEM and micromagnetic study of FePt ordered/disordered exchange spring media

Ausgeführt am Institut für Festkörperphysik
der Technischen Universität Wien

unter der Anleitung von

Univ. Prof. Dipl. -Ing. Dr. Techn. Josef Fidler

durch

Barbara Dymerska

Goldeggasse 20/2
1040 Wien

Wien, am 08 May 2012

*Any knowledge that doesn't lead to new questions quickly dies out:
it fails to maintain the temperature required for sustaining life.*

- Wisława Szymborska -

Kurzfassung

Im Rahmen der folgenden Arbeit wurden "exchange-spring" Medien untersucht. Dies sind Materialien in welchen hart- und weichmagnetische Schichten stark miteinander austauschwechselwirken. Als Beispiel für ein solches Medium wurde eine Nanostruktur aus FePt L1₀/A1 Dünnenschichten analysiert. Diese Untersuchung ergab, dass sich zwischen der chemisch geordneten L1₀-Phase und der ungeordneten A1-Phase eine komplexe und raue Grenzfläche ausbildet. Aus den gemessenen Hysteresiskurven und der HRTEM Analyse lässt sich zudem schlussfolgern, dass die Rauigkeit der Grenzfläche einen Einfluss auf die Schalteigenschaften des Materials hat. Um herauszufinden, wie solch eine Grenzfläche das Ummagnetisierungsverhalten des Mediums beeinflusst, wurden mikromagnetische Simulationen durchgeführt. Für die Simulationen wurden markante Merkmale, so wie Obstakel der einen Phase eingebettet in der anderen Phase, übertragen in Finite Element Modelle. Zusätzlich wurde die Verteilungsfunktion der hartmagnetische Phase entlang der Probehöhe untersucht. Numerische Berechnungen ergaben, dass Position und Größe der Obstakeln einem entscheidenden Einfluss auf das Schaltverhalten des Materials haben. Je nach den Herstellungsparametern der Probe ließ sich die Funktion linear, logistisch oder quadratisch fitten. Für eine quadratische L1₀-Phase in einer 18 nm breiten Grenzfläche ergaben die Berechnung als kleinstes mögliches Schaltfeld $H_{sw} = 0.9$ T. Die numerischen Resultate stimmen gut überein mit einer analytischen Formel für das Verankerungsfeld, welche hergeleitet wurde für den allgemeinen Fall räumlich veränderlicher Magnetisierung, Anisotropie und Austauschkonstante. Weiterführende Arbeit könnte sich mit der Wechselwirkung zwischen magnetischen Körnern sowie der Simulation von Lese-/Schreibprozessen in Bit-gemusterten Materialien befassen. Abschließend ist hervorzuheben, dass sich die Resultate dieser Arbeit nicht nur auf FePt L1₀/A1 Dünnenschichten auwenden lassen, sondern auch interessant sein könnten für andere exchange-spring Materialien, z.B. CoPt L1₀/A1 oder FePt(L1₀)/FeAu(L1₀).

Abstract

In this work exchange spring media are discussed. Within such materials there exist magnetically hard and soft layers which are strongly exchange coupled. As an example a nanostructure of FePt L1₀/A1 thin films is analysed with electron microscopy. A complex rough interphase between the chemically ordered L1₀ and disordered A1 phase was discovered. This observation together with the experimental analysis of hysteresis loops lead to the conclusion, that a change of the interphase profile roughness by a few nanometers alters significantly the switching properties of FePt L1₀/A1 media. In order to find the physical processes responsible for this behaviour, micromagnetic simulations have been carried out. For the purpose of the simulations, observed features, such as obstacles of one phase embedded in the matrix of a second phase, were transferred into finite element models. Numerical calculations show that the position and size of the obstacles significantly alters the switching field of the media. Also the experimental distribution of the hard phase along the thickness of the medium was analysed. It was found to fit linear, logistic or quadratic functions in the interphase region, depending on the sample deposition conditions. The minimal switching field of $H_{sw} = 0.9$ T was calculated for a quadratic L1₀ distribution in a 18 nm thick interphase region. The above mentioned numerical results agree well with an analytical formula for the pinning field of the exchange spring media, which is derived for the general case of spatially varying magnetization, anisotropy and exchange constant. In future work the analysis could be extended to a study of an interaction between magnetic grains and simulation of a read/write processes for a fully formulated FePt bit patterned media. It is emphasized that the applicability of the results is not limited to FePt L1₀/A1 films but could be interesting also for other exchange spring media, such as CoPt L1₀/A1 or FePt(L1₀)/FeAu(L1₀).

Contents

1	Introduction	1
2	Fundamentals	3
2.1	Magnetic properties of the materials	3
2.1.1	Ferromagnetism	4
2.1.2	Magnetic Gibbs free energy	5
2.1.3	Domain walls	7
2.2	Perpendicular magnetic recording	8
2.2.1	Superparamagnetic limit	9
2.2.2	Exchange spring media	10
2.3	Properties of FePt	11
2.4	TEM material analysis methods	14
2.4.1	Bright Field imaging	14
2.4.2	Diffraction Pattern	15
2.4.3	Dark Field imaging	16
2.4.4	Scanning TEM and EDX	17
2.5	Finite element micromagnetic method	18
3	SEM/TEM study	21
3.1	Origin of the FePt films	21
3.2	TEM sample preparation	23
3.3	Results and discussion	25
4	Micromagnetic study	40
4.1	Derivation of the pinning field	40
4.2	Nanomagnetic modelling	44
4.3	Results and discussion	51
5	Summary	61
A	Appendix	63
	References	66

1 Introduction

During the last decade exchange coupled media have been theoretically proposed [1], [2] and experimentally realized [3] for perpendicular magnetic recording. The principle discussed in the above cited papers relies on a multilayer structure combining magnetically hard and soft materials. This leads to significant reduction of the coercive field (H_c) in comparison with a single hard layer while keeping sufficient thermal stability. Two approaches were introduced in order to get the optimal properties: In the first one, Victora and Shen assumed a coherent switching of the magnetization. In order to decrease H_c in such model the exchange coupling between the hard and soft layer must be reduced by an additional spacing interlayer [1].

In the second approach, Suess et al. proposed an incoherent switching mechanism with a domain wall nucleation in the soft phase and propagation into the hard phase [4]. This is valid if the domain wall width of the hard layer is smaller than the soft layer thickness. It was proved that the hard and the soft phase should be strongly exchange-coupled in order to obtain the highest reduction of the coercivity. For this reason no spacing interlayer should be introduced [5].

Furthermore, a model with a continuously decreasing magnetocrystalline anisotropy constant (K_1) along the thickness of the film was proposed instead of a hard/soft step-like K_1 -transition [6]. This leads to an even greater reduction of the H_c at the same thermal stability. One of the experimental attempts to obtain such a smooth gradient of the anisotropy was described by Alexandrakis et al [7]. Here, FePt was deposited on (001) textured MgO substrate, which was continuously cooled down during the process. This manipulates the crystallographic structure of FePt and thus also its anisotropy. Together with numerical studies of thermodynamic properties of FePt alloys [8] this work was an inspiration for Lee et al. to create a model with a rough interface boundary [9]. In contrary to the original idea of graded media, this model consists only of two phases: hard magnetic, chemically ordered, fct, L1₀ phase and soft magnetic, chemically disordered, fcc, A1 phase. It was assumed that nucleation sites of the A1 phase appear in the L1₀ phase at a certain temperature. During further cooling of the substrate the soft phase starts to grow at these sites. Finally, a rough wedge-shaped L1₀/A1 interphase is formed. For a comparison also a stacked medium with gradually changing anisotropy constant was created. Both models showed similar switching behaviour.

In this thesis exchange spring media are treated from the experimental and theoretical point of view. FePt L1₀/A1 films are investigated by means of an electron microscopy. Discovered nanostructures were transferred into Finite Element Micromagnetic models and magnetic reversal processes were simulated.

Fundamentals included in the second chapter of this thesis describe basic properties of ferromagnetic materials. All of them will be subsequently discussed in details for the exchange spring media. Also the main concept of the magnetic recoding is explained, since a main application of the FePt L1₀/A1 films is for the hard disc industry. Additionally, all the TEM material analysis methods are shortly described, which allow to follow reasoning in the experimental part of this thesis. Moreover, a summary about the Finite Element Method is presented for a better understanding of the numerical simulations.

The second chapter is devoted to the structural analysis of the FePt L1₀/A1 thin films. How the samples were produced and prepared for the TEM analysis is included in the beginning of the chapter. Subsequently Scanning Electron Microscopy and Tunnelling Electron Microscopy investigation results are presented. The third chapter contains the theoretical discussion about the exchange spring media. Firstly, an analytical formula is derived describing the pinning at the rough interphase. Secondly, numerical micromagnetic simulations are performed with finite element models representing characteristic nanostructure of the exchange spring media. Obtained results: magnetisation curves and domain wall motion images are presented and discussed.

Finally, in the last fifth chapter a short summary of the work will be given as well as an outlook for the possible future applications of the established conclusions and derived theory.

2 Fundamentals

2.1 Magnetic properties of the materials

Magnetism is a physical property of a matter, which manifest itself by a reaction of the material to the applied magnetic field. An easy example is an attraction or repulsion force between two magnets. Magnetism arises in an atom from three sources [10]:

1. electron orbital angular motion around the nucleus
2. electron magnetic dipole moment caused by an intrinsic property of a spin
3. nuclear magnetic moment

Electrons can move only along discrete orbits around nucleus. These orbits are denoted by azimuthal quantum number $l = 0, 1, 2, \dots$. Moreover, electrons as fermions have spin angular momentum quantum number, equal to one of the two possible values: $s = \pm 1/2$. Due to a strong orbit-orbit and spin-spin interactions the resultant atomic momenta equal to

$$S = \sum_i s_i \quad L = \sum_i l_i, \quad (1)$$

where the sum runs over all electrons in the atom. Above described discretisation of an atomic electron system leads to the quantisation of the magnetic moment of an atom (μ_{atom}), which can be written in the Bohr magneton units (μ_B),

$$\mu_{atom} = g_J \mu_B \sqrt{J(J+1)}, \quad \mu_B = \frac{e\hbar}{2m}, \quad (2)$$

where $J = S + L$ is the total angular momentum of an atom and g_J is the Lande factor,

$$g = 1 + \frac{J(J+1) + S(S+1) - L(L+1)}{2J(J+1)}. \quad (3)$$

The last source of the magnetic properties in the matter, the nuclear magnetic moment, is around 1800 times smaller than Bohr magneton. Therefore, its contribution to the material magnetisation is negligible.

The total magnetisation of the material is defined as a number of atomic magnetic moments (N) per volume (V) unit,

$$\mathbf{M} = \frac{N\mu_{atom}}{V} \left[\frac{\text{Am}^2}{\text{m}^3} \right] \quad (4)$$

2.1.1 Ferromagnetism

Unlike the paramagnetic atoms, which interact only with external field, the atomic spins in ferromagnetic materials interact with each other [11]. It is so called exchange interaction, which is responsible for creating magnetic domains within a material. The response of a ferromagnetic material (\mathbf{M}) to an external field (\mathbf{H}) can be described by,

$$\mathbf{M} = \chi\mathbf{H}, \quad (5)$$

where $\chi = \chi(\mathbf{H})$ is a field dependent magnetic susceptibility. With this definition an equation for magnetic flux density can be written as following,

$$\mathbf{B} = \mu_0(\mathbf{H} + \mathbf{M}) = \mu_0(1 + \chi)\mathbf{H} = \mu_0\mu_r\mathbf{H}, \quad (6)$$

where $\mu_r = \mu_r(\mathbf{H})$ is a field dependent magnetic permeability. In ferromagnetic case magnetic susceptibility and permeability fulfil the relations [12],

$$\chi(\mathbf{H}) \gg 0, \quad \mu_r(\mathbf{H}) \gg 1. \quad (7)$$

In such materials the value of the magnetisation depends on the history of the applied field. A typical dependency is shown in Fig.1, where this component of the magnetisation is plotted, which is in the direction of the magnetic field: M_H .

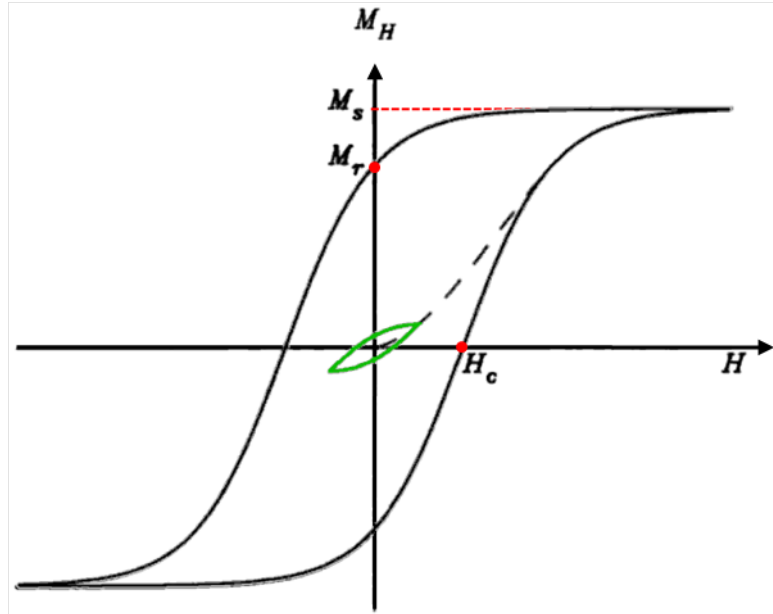


Figure 1: An example of a hysteresis curve of a typical ferromagnetic material [11]. The dashed black line represents a virgin curve. The green line is a minor hysteresis loop. The outermost black curve is a so called limiting hysteresis curve. Additionally, the saturation (M_s), the remanence (M_r) magnetisations and the coercive field (H_c) are marked.

The limiting hysteresis curve (Fig.1 outermost black loop) is obtainable by applying a sufficiently large field in one direction, decreasing it to zero and then increasing it to a large value in the opposite direction. This plot can be reproduced in successive cycles of the external field. In this work all the hysteresis curve figures present only one branch of the limiting curve since it shows all the complementary informations. The second branch is a pure translation by $2H_c$ of the first branch along H -axis. The dashed black line in the diagram represents the so called virgin magnetisation curve, which is only obtainable if the sample is previously demagnetised (has $M = 0$ at $H = 0$). If, however, the field applied to the demagnetised sample is not strong enough to reach the limiting curve, the magnetisation can follow a minor hysteresis loop (green curve).

Additionally three characteristic quantities are marked in Fig.1. The remanence magnetisation (M_r) is a magnetisation, which ferromagnetic material posses in an absence of the external field. Saturation magnetisation (M_s) is the maximal achievable magnetisation for a given material. The last quantity, coercive field (H_c) is the intensity of the external field, which has to be applied in order achieve $M = 0$, when initially the material was magnetically saturated. Materials with low H_c are denoted as magnetically soft and one with high H_c magnetically hard.

Moreover a switching field (H_{sw}) can be defined as a maximum of a magnetisation first derivative with respect to the applied field,

$$H_{sw} = \max \left(\frac{\partial M_H(H)}{\partial H} \right). \quad (8)$$

This quantity says how strong the external field must be in order to reverse the magnetisation from up to down or vice versa.

2.1.2 Magnetic Gibbs free energy

A short description of a thermodynamics in magnetics will be helpful for a better understanding of the conclusions raised in sections 4.1 and 4.3. An inner energy of a ferromagnetic material can be described by a Gibbs free energy, which consists of several terms: exchange, magnetocrystalline anisotropy, Zeeman, stray field and deformation energy.

Since in this work magnetostrictive effects are not considered the deformation energy is neglected. Moreover, the coercive field of the exchange spring media does not change significantly when the stray field component is included [6]. This leaves only three terms of the energy for the discussion,

$$E_{Gibbs} = E_{ex} + E_{ani} + E_{Zeeman}. \quad (9)$$

a) Exchange energy: E_{ex}

The exchange interaction between ionic spins in a ferromagnetic metal is described by Heisenberg Hamiltonian:

$$H_{ex} = - \sum_{i=j} J_{ij} \mathbf{S}_i \cdot \mathbf{S}_j, \quad (10)$$

where J_{ij} is exchange integral between spins \mathbf{S}_i and \mathbf{S}_j .

If only interactions with the closes neighbours are considered, the exchange integrals can be substituted by a constant value: J_0 . Assuming additionally that all the ionic spins have the same magnitude S , the exchange energy density can be written as following,

$$E_{ex} = A \int_V \sum_i (\nabla u_i)^2 dV, \quad (11)$$

where u_i is a unit vector in the spin direction and V is the total volume of the material. The coefficient A is so called exchange stiffness constant, which depends on the type of ions and the lattice in which they are located. As an example, for a cubic primitive lattice with lattice constant a it holds,

$$A = \frac{2J_0 S^2}{a}. \quad (12)$$

b) Magnetocrystalline anisotropy energy: E_{ani}

Magnetocrystalline anisotropy describes the dependency of the system inner energy on the direction of its magnetisation. This energy term has the same symmetry as the crystal lattice. The directions for which the energy is minimised are called easy axes.

For sake of simplicity, in this work FePt media are assumed to have uniaxial anisotropy along the z-axis perpendicular to the film plane. This is only true for the $L1_0$ ordered phase, whereas $A1$ disordered phase has in reality a cubic anisotropy. The uniaxial magnetocrystalline anisotropy energy can be expresses by power series of $\sin^2 \theta$, where θ is an angle between the easy axis and the magnetisation direction,

$$E_{ani} = \int_V (K_1 \sin^2 \theta + K_2 \sin^4 \theta + \dots) dV. \quad (13)$$

In our discussion only the first term, with anisotropy constant K_1 , is considered.

Zeeman energy: E_{Zeeman}

A magnetostatic energy gained by a ferromagnetic material due to the existence of an external magnetic field is called Zeeman energy,

$$E_{Zeeman} = - \int_V \mu_0 \mathbf{M}_s \cdot \mathbf{H}_{ext} dV = - \int_V \mathbf{J}_s \cdot \mathbf{H}_{ext} dV. \quad (14)$$

Here $J_s = \mu_0 M_s$ is a saturation polarisation.

Conclusively, after above described assumptions the total Gibbs free energy reads,

$$E_{Gibbs} = \int_V \left(A \sum_i (\nabla u_i)^2 + K_1 \sin^2 \theta - J_s H_{ext} \cos \theta \right) dV \quad (15)$$

More detailed description of the magnetic free energy components together with their derivation can be found in [13].

2.1.3 Domain walls

Magnetic domains are regions in a ferromagnetic material which possess uniform spontaneous magnetisation. Neighbouring magnetic domains are separated by a transition region called domain wall, where spins gradually change their direction from one domain to the other. Depending how the spins behave in this transition region one can differ between two main types of the domain wall named after physicists: Bloch and Neel [13].

Neel walls occur in a very thin films for which the exchange length (a range of the exchange interactions) is bigger than the thickness of the film. In such case the magnetisation rotates from one domain to the other around the axis parallel to the domain wall plane.

The mentioned exchange length can be calculated according to,

$$l_{ex} = \min \left(\sqrt{\frac{A}{K_1}}, \sqrt{\frac{A}{(J_s^2/\mu_0)}} \right). \quad (16)$$

For FePt A1 phase this gives: $l_{ex,A1} = 15.9$ nm and for L1₀: $l_{ex,L1_0} = 4.5$ nm, which in both cases is less than the total film thickness (see section 3.1). In such case the Bloch wall can be considered, where the transition happens by a rotation of the magnetisation around the axis perpendicular to the wall plane (Fig.2).

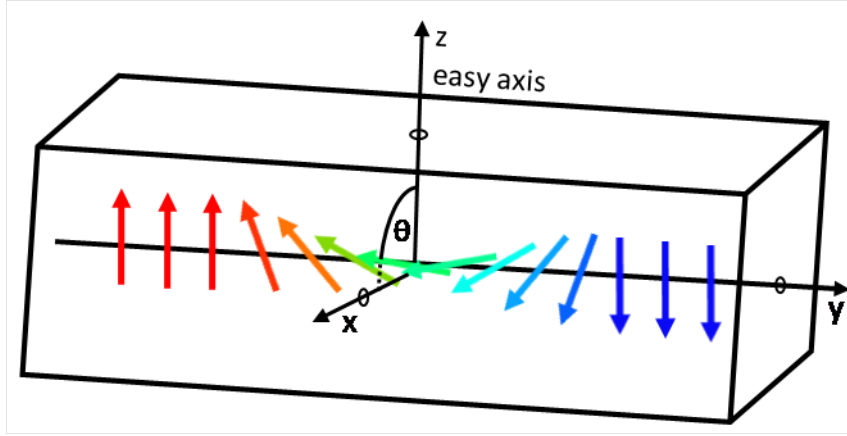


Figure 2: Symbolic representation of the magnetisation rotation in a 180° Bloch domain wall. The rotational y-axis is perpendicular to the domain wall plane and to the easy axis of the material.

In uniaxial anisotropy materials the rotation angle within the Bloch domain wall is always 180° . The energy stored by such wall reads,

$$E_{DW} = 4\sqrt{AK_1}, \quad (17)$$

assuming that magnetocrystalline anisotropy constant $K \cong K_1$.

2.2 Perpendicular magnetic recording

Thin FePt $A1/L1_0$ films belong to a group of exchange spring media, which are utilized in a perpendicular magnetic recording technology. This technology has mostly an application in a hard disc industry. It is substantial to get familiar with a main concept of the perpendicular magnetic recording in order to understand the importance of such properties as high thermal stability and low switching field of the FePt films.

In Fig.3 a read/write process in the perpendicular medium is schematically sketched. The recording medium is composed of an array of basic units of information: bits. They store an information: true or false (1 or 0) in a shape of magnetic grains with magnetisation up or down respectively. The magnetisation direction is always perpendicular to the medium plane: that is exactly the direction of the uniaxial anisotropy of the film.

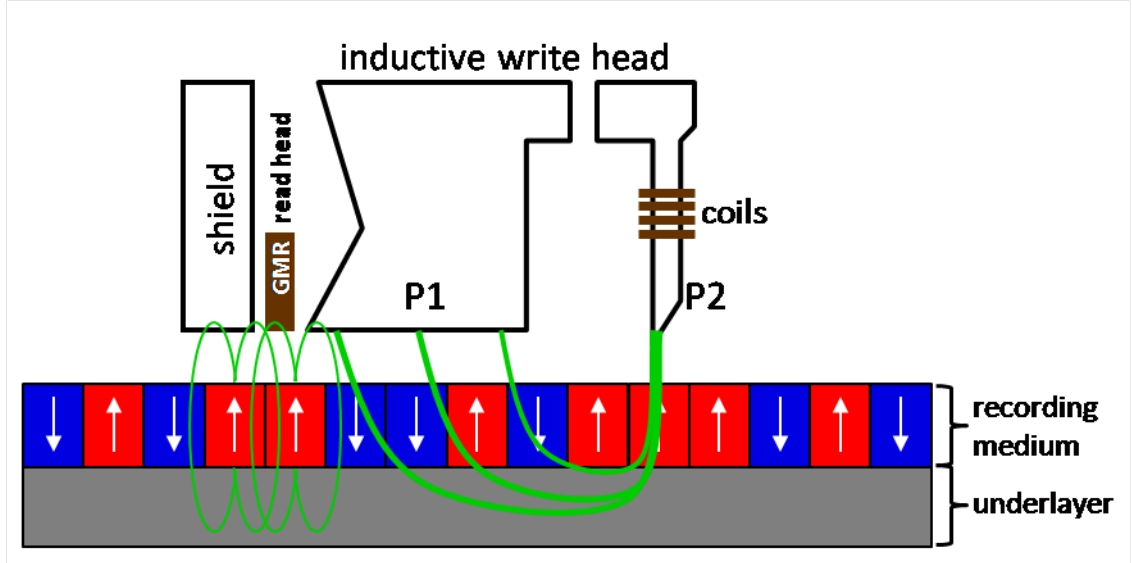


Figure 3: A schema of the read/write process. Elements of the magnetic medium and the read/write head are marked directly in the figure. Shortcuts P1 and P2 corresponds to the two poles of the writing head. Thin green lines represent stray fields of the magnetised grains, thick ones show a magnetic flux of the write head.

For readout Giant Magneto-Resistant (GMR) sensors are used, which feel the stray field of the grains (Fig.3 thin green lines). For rewriting the bits an inductive write head is used. It consist of two poles. A magnetic flux (thick green lines) comes from the first pole (P1), penetrates the medium and is focused on the second pole (P2). Close to P2 the flux is strong enough to reverse the grain. This happens if the magnetisation points in the opposite direction than the field created by the head.

2.2.1 Superparamagnetic limit

A trend to increase the areal density of the recording media brought a problem of superparamagnetic limit: When a ferromagnetic grain size is strongly reduced the thermal fluctuations at a room temperature ($k_B T_{300}$) overcome the energy barrier (ΔE) between up and down magnetisation states. This leads to a spontaneous switching between these two states and the bit information is no longer stored.

The following Fig.4 presents potential curves for two grains differing only in size. Figure 4 a) represents the bigger grain, for which energy barrier between two magnetic states (red and blue arrows) is significantly larger than the thermal energy. For the smaller grain, represented by Fig.4 b), the energy levels of the magnetisation up (E_{\uparrow}) and down (E_{\downarrow}) stay the same, only the barrier between them is smaller due to the volume reduction. Since thermal energy is larger than ΔE the grain switches spontaneously (symbolised by an arched black arrow).

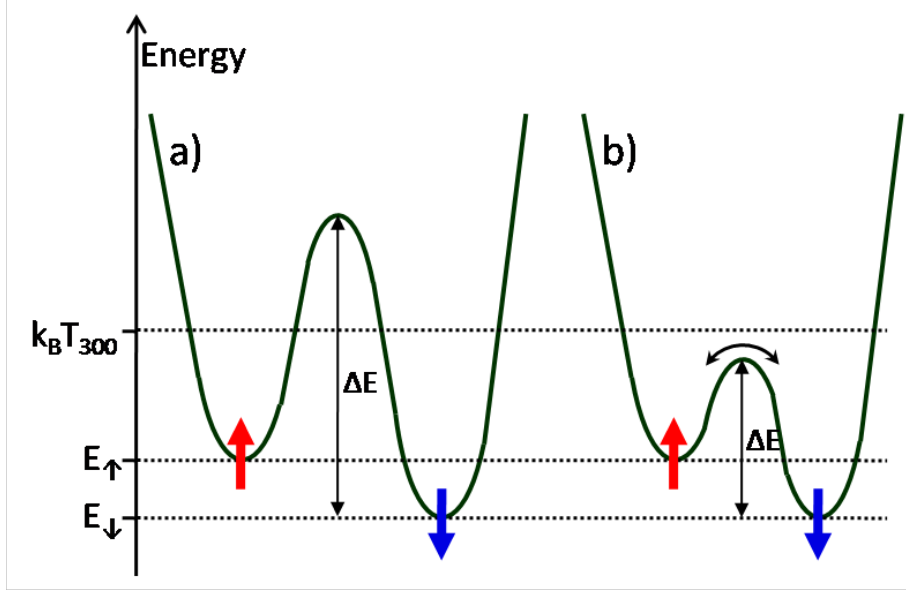


Figure 4: Potential curves (green) of two magnetic grains. Red and blue arrows represent two possible magnetisation states. Thermal, spin up and down energies ($k_B T_{300}$, E_{\uparrow} and E_{\downarrow} respectively) are indicated on the energy scale. a) Grain with sufficient volume so that the energy barrier ΔE is larger than $k_B T_{300}$. b) Smaller grain with $\Delta E \ll k_B T_{300}$.

Above mentioned energy barrier of a single domain grain is described by a following proportionality,

$$\Delta E \sim KV, \quad (18)$$

with V being the grain volume and K the magnetocrystalline anisotropy constant. According to this equation the reduction of the bit size can be compensated by an increase of the anisotropy constant [4]. This can however lead to a too large anisotropy field of the magnetic grain,

$$H_{ani} = \frac{2K_1}{J_s} \quad (19)$$

so that the head with a limited writing field would be unable to switch the magnetisation. A solution for this problem exists in a form of an exchange spring media.

2.2.2 Exchange spring media

Exchange spring media concept is based on an idea of combining together magnetically soft and hard layers [1],[2]. If these layers are strongly exchange coupled a significant reduction of the coercive field of the whole structure occurs. The thermal stability remains, however, at the level of the magnetically harder material. This phenomenon is visualised in Fig.5. The potential curve (green line) of a single

hard layer (Fig.5 a)) has a very steep slope between the two possible magnetisation states (up and down). This means that the gradient of this potential is very high. The force, which has to be applied, is proportional to this gradient, hence the external magnetic field has to be very high in order to switch such structure. For the exchange spring media (Fig.5 b)) the slope of the potential curve is reduced by coupling the soft layer with the hard layer. The energy barrier, however, stays the same as in case a) [14].

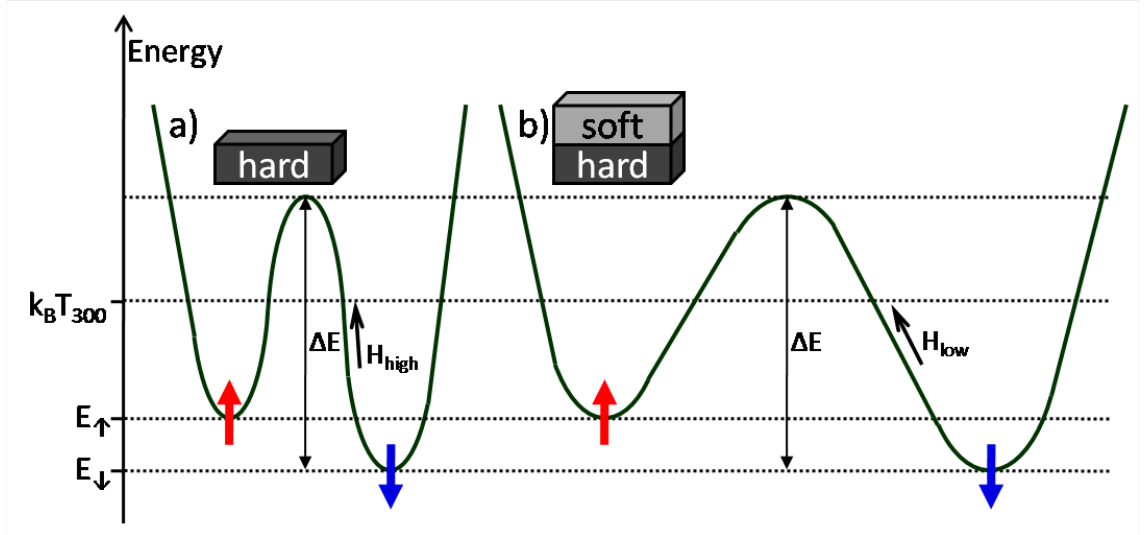


Figure 5: Potential curves (green) of a) a single hard layer, b) exchange coupled hard and soft layer. Red and blue arrows represent two possible magnetisation states. For both media the energy barrier (ΔE) is the same. A steeper slope of the energy curve represents higher switching field (H_{high}). Thermal, spin up and down energies ($k_B T_{300}$, E_{\uparrow} and E_{\downarrow} respectively) are indicated on the energy scale [14].

A good material candidate for the exchange spring media is FePt. It is possible to couple two of its phases: magnetically soft, disordered A1 and much harder, ordered L1₀. More detailed characterisation of this material is presented in the following section.

2.3 Properties of FePt

The following Fig.6 presents a phase diagram of FePt alloys. There are three stable chemically ordered structures: Fe₃Pt (γ_1), FePt₃ (γ_3) and FePt (γ_2), also known as FePt L1₀. Above their transition temperatures, a metastable disordered structure exists (γ Fe,Pt). This phase also occurs if the material is deposited at a room temperature and is denoted as FePt A1. Since we are interested in both A1 and L1₀ phases the deposition has to be done in an elevated temperatures with a subsequent cooling. Detailed description of the sputtering processes is given in section 3.1.

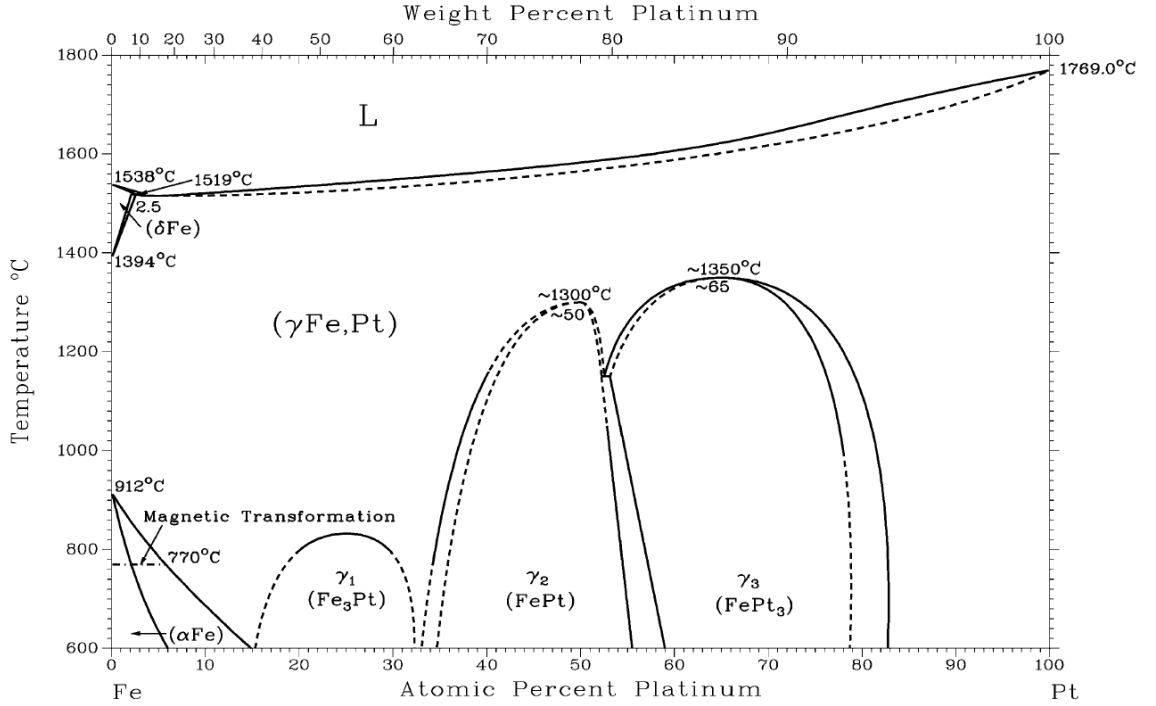


Figure 6: FePt alloys phase diagram from Ref.[15]

A first difference between (γ Fe,Pt) and (γ_2 FePt) lies in their crystallographic structure. Disordered A1 phase has a face-centered cubic (fcc) unit cell within which Fe and Pt are randomly distributed (Fig.7 a). According to [16], experimentally measured (X-ray diffraction) lattice constant of FePt fcc is equal to $a = 3.820 \text{ \AA}$. This value agrees well with the one obtained by Java Electron Microscopy Simulation (JEMS) software, equal to $a = 3.861 \text{ \AA}$ (Tab.1).

The L1₀ phase is composed of alternating layers of Fe and Pt (Fig.7 b). Since these elements have different atomic radii (140 pm and 135 pm respectively), such ordered structure possesses face-centered tetragonal (fct) unit cell. The lattice parameters found in [17] reads: $a = 3.850 \text{ \AA}$ and $c = 3.693 \text{ \AA}$, while the simulated one by JEMS are equal to: $a = 3.852 \text{ \AA}$ and $c = 3.713 \text{ \AA}$, which again is consistent. The values found in the Tab.1 will be used in the TEM experimental part (section 3.3) for the recognition of the phase and orientation of the crystallographic structure.

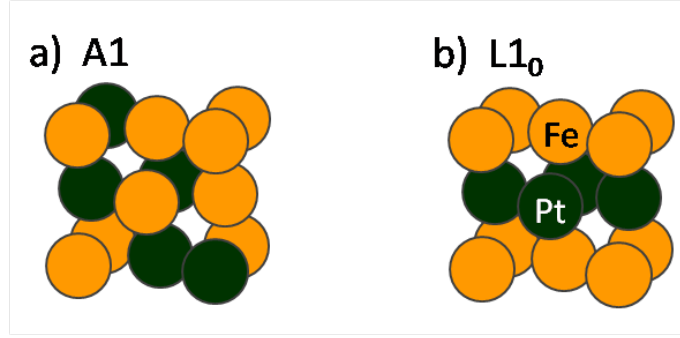


Figure 7: FePt unit cells of a) a disordered A1 and b) an ordered L1₀ phase. Green atoms symbolise Pt, yellow: Fe.

FePt A1				FePt L1 ₀			
h	k	l	distance [Å]	h	k	l	distance [Å]
1	0	0	3.8160	0	0	1	3.7130
0	0	1	3.8160	1	1	0	2.7238
1	1	0	2.6983	1	1	1	2.1962
1	0	1	2.6983	2	0	0	1.9260
1	1	1	2.2032	0	0	2	1.8565
2	0	0	1.9080	2	0	1	1.7097
0	0	2	1.9080	1	1	2	1.5341
2	1	0	1.7066	2	2	0	1.3619
2	1	1	1.5579	2	0	2	1.3366
2	2	0	1.3492	2	2	1	1.2786

Table 1: Lattice constants for FePt A1 and L1₀ phases obtained from Java Electron Microscopy Simulation (JEMS) software.

Due to above mentioned differences in the structure also the magnetic properties of the two FePt phases vary significantly. The A1 phase has a relatively small magnetocrystalline anisotropy along [001] axis in comparison with L1₀ phase: $K_1 = 10^5 \text{ J/m}^3$ versus $K_1 = 5 \cdot 10^6 \text{ J/m}^3$. This means, that for a very thin films the shape anisotropy within the A1 phase dominates and the easy axis points parallel to the film plane. In contrary, the L1₀ phase, with 50 times bigger K_1 , keeps the easy axis along [001] direction. This strong magnetocrystalline anisotropy is explained by a spin-orbit coupling of Pt in combination with a hybridisation between Fe 3d and Pt 5d orbits [18]. More information, for instance about chemical ordering of both FePt phases can be found in [19].

2.4 TEM material analysis methods

Transmission Electron Microscopy is a very powerful method for the chemical and crystallographic analysis of diverse materials. In order to understand obtained results for FePt (section 3.3) one need to get familiar with the basic working principle of such microscope. TEM utilizes as a primary source highly energetic electron beam, which is focused by a system of electromagnetic coils and directed onto a sample. Electrons that passed through a material are either:

- transmitted without diffraction (so called zero beam)
- diffracted (elastically scattered at the crystallographic planes)
- inelastically scattered

The chosen TEM working mode: Bright Field (BF), Dark Field (DF) or Diffraction Pattern (DP), depends on which part of the secondary electrons is detected.

2.4.1 Bright Field imaging

In the Bright Field imaging transmitted electrons are used. The contrast is obtained by positioning an aperture in such way that it removes the diffracted electrons from the detection area (Fig.8). However, even without contrast aperture some of the electrons are scattered away (eg. are caught by a pole pieces), hence there is always a finite minimal contrast. In the BF image thicker areas of the sample are darker, thinner lighter. A sufficiently strong magnification allows to observe lattice symmetries. This is so called High Resolution TEM (HRTEM).

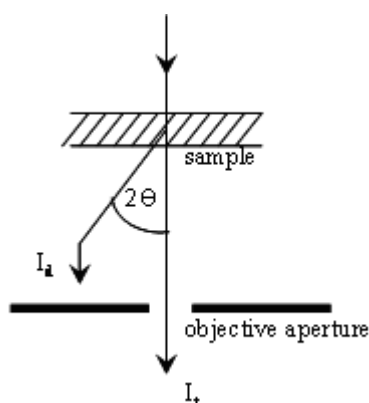


Figure 8: Bright field imaging mode: the transmitted beam (I_t) passes through the objective aperture, whereas the diffracted on (I_d) is removed from the detection area.

2.4.2 Diffraction Pattern

Diffraction patterns contains information about the crystallographic properties of the sample. One can find out about symmetries, lattice parameters or structural defects within the material. Additionally, it is possible to determine the orientation of the grains, their sizes and if their are single of multiphase. The DP always contains the electrons from the whole illuminated area of the sample. In order to obtain a local information Selected Area (SA) apertures are used.

Obtained DP images are difficult to analyse if no prior study was done about the material in interest. Such information as elemental composition, possible phases of the material simplify the investigation.

Based on the origin of the samples (described in the section 3.1) we could assume in this work, that we deal with the following structures: MgO substrate and FePt in A1 and L1₀ phase. Web Electron Microscopy Applications Software (WebEMAPS) [20] was used in order to simulate SADP of the film composed of this three phases. Figure9 shows obtained results for a plain view diffraction pattern with [001] as a zone axis (Fig.9 a) and a cross section DP with [0-10] as a zone axis (Fig.9 b)).

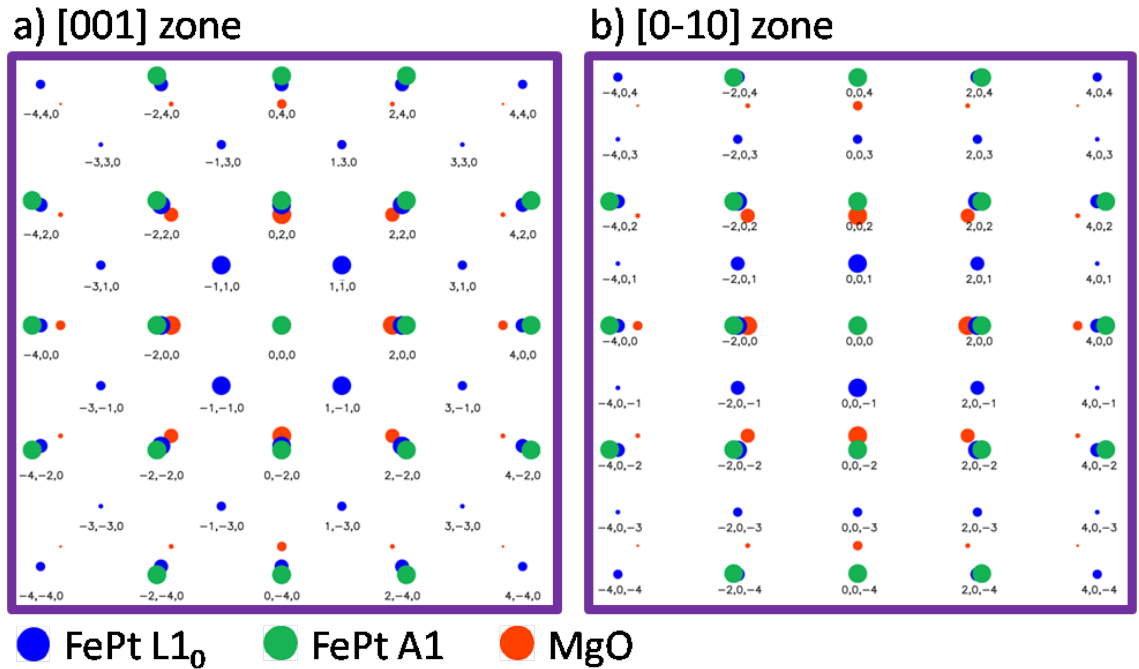


Figure 9: Simulated Selected Area Diffraction Patterns (SADP) for FePt L1₀/A1 on MgO substrate. a) DP for a plain view with [001] as a zone. b) DP for a cross section view with [0-10] as a zone.

Both patterns shown in Fig.9 are created assuming that the primary electrons were diffracted only once on their path. It can, however, happen that they get rediffracted for the second time. It is especially possible if the sample is heterogeneous; for

instance consists of two layers of significantly different materials. This is the case for FePt on MgO substrate. A schematic visualisation how such double DP is created is presented in Fig.10. Figure 10 a) shows patterns for materials consisting only of crystal A or B, whereas Fig.10 b) presents a simple superposition of this patterns if the sample consists of both crystals, but all the electrons were diffracted only once. In Fig.10 one of the beams diffracted on crystal B gets diffracted again on crystal A. Finally, Fig.10 d) shows a fully formulated double diffraction pattern for a layered structure consisting of crystal B at the top of crystal.

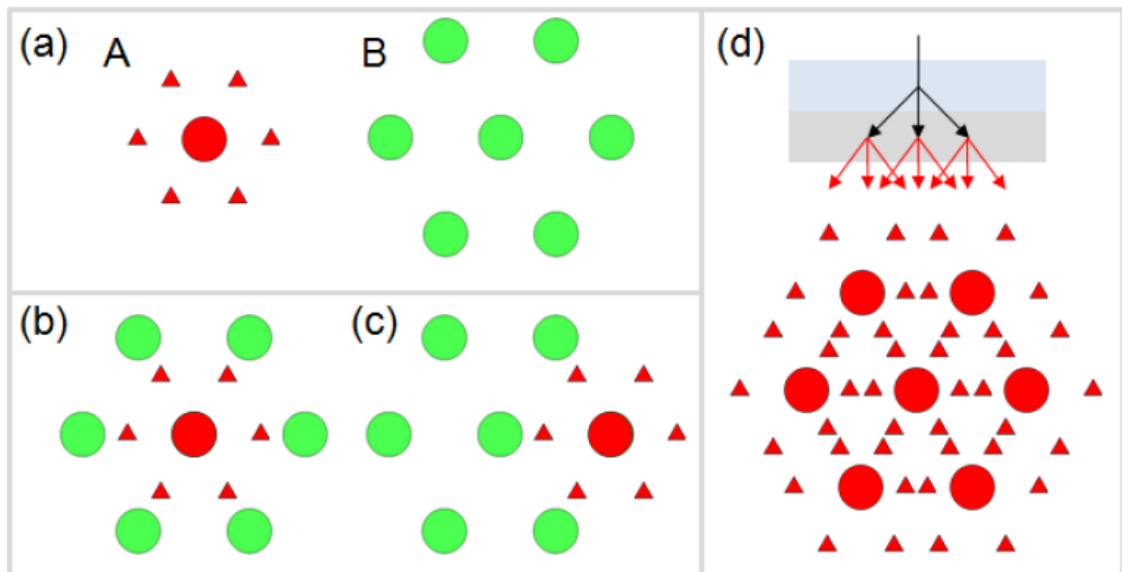


Figure 10: a) Diffraction pattern of a single crystal of a type A or B. b) Superposition of the single diffraction patterns for a material consisting of A and B. c) Diffraction pattern superposition for the case that one of the beams diffracted by crystal B is rediffracted on the crystal A. d) Double diffraction pattern. The images was taken from [21].

Comparison of the simulated images with experimental data allowed to mark crystallographic orientations of the grains and families of lattice planes for FePt samples.

2.4.3 Dark Field imaging

In the Dark Field imaging an objective aperture is centred around a selected DP spot. The electron beam is tilted in such way that the chosen diffracted beam is parallel to the optical axis of the microscope (Fig.11). As a result an image of the sample is created. In contrary to the bright field image, only these structures on the material are bright which have a given crystallographic orientation and belongs to a certain material defined by the chosen DP spot. This method is very useful for a mapping of phase distributions within the sample (see Fig.25 or 26).

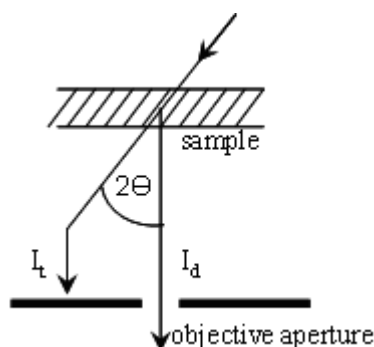


Figure 11: Dark Field imaging: the primary beam is tilted so than the diffracted beam (I_d) passes through the objective aperture, whereas the transmitted one (I_t) get removed from the detection area.

2.4.4 Scanning TEM and EDX

In the Scanning mode of TEM (STEM) the electron beam is focused onto the sample. This allows to investigate areas of several nanometers. Such merged beam scans the region of interest. Due to a higher electron intensity it is possible to investigate in STEM thicker samples than in TEM.

In this working mode a localised elemental analysis of the material can be done. For this Energy Dispersive X-ray spectroscopy is utilized. Inelastic scattering of the primary beam (Fig.12 (1)) can result in displacing of electrons from the inner atomic shells within the sample (Fig.12 (2)). This leads an atom in excited state. A relaxation occurs by filling of the vacancy with an electron from the outer atomic shell (Fig.12 (3)). An element characteristic X-ray emission is incidental to this process (Fig.12 (4)). Emitted photons can be collected and analysed.

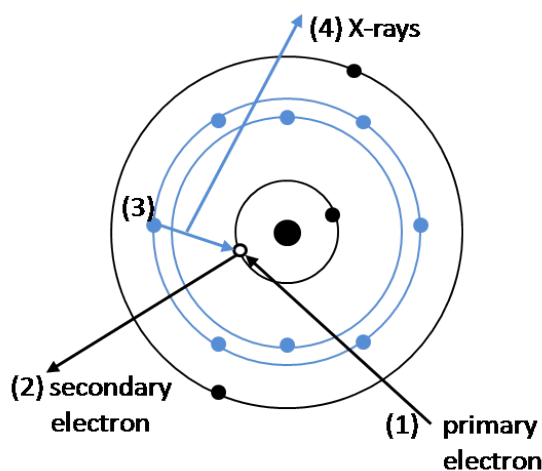


Figure 12: A schematic visualisation of an X-ray emission from an atom. The numbers from (1) to (4) show the order of the occurring processes.

2.5 Finite element micromagnetic method

Finite Element Method (FEM) is a numerical technique of solving partial differential equations, hence it is widely used for such applications as visualisation of material deformation (aeronautical, automotive industry) or heat transport (civil engineering). It is also suitable for a study of the magnetisation dynamics in ferromagnetic materials. A precessional movement of the magnetic polarisation around the effective field direction with damping in a ferromagnetic environment is described by Landau-Lifshitz-Gilbert (LLG) equation,

$$\frac{\partial \mathbf{J}}{\partial t} = -\frac{|\gamma|}{1+\alpha^2} \mathbf{J} \times \mathbf{H}_{\text{eff}} - \frac{\alpha}{1+\alpha^2} \frac{|\gamma|}{J_s} \mathbf{J} \times (\mathbf{J} \times \mathbf{H}_{\text{eff}}), \quad (20)$$

where following quantities are used:

$\mathbf{J} = \mathbf{J}(\mathbf{r}, t)$ - magnetic polarisation vector (equal to $\mu_0 \mathbf{M}(\mathbf{r}, t)$),

$\mathbf{H}_{\text{eff}} = \mathbf{H}_{\text{eff}}(\mathbf{r}, t)$ - effective field,

\mathbf{r} - position vector,

$|\gamma| = 2.2102 \cdot 10^5$ [m/As] - electron gyromagnetic ratio,

α - Gilbert damping constant.

One can discretize the above equation by choosing a suitable expansion of the polarisation $\mathbf{J}(\mathbf{r}, t)$ with basis functions $\varphi_i(\mathbf{r})$ [22],

$$J^{x,y,z}(\mathbf{r}) \approx J_s(\mathbf{r}) \sum_{i=1}^n u_i^{x,y,z} \varphi_i(\mathbf{r}). \quad (21)$$

The coefficients $u_i^{x,y,z}$ are the components of the normalised spontaneous polarisation at the node point i , hence

$$\sum_{i=1}^n u_i^{x,y,z} = 1 \quad (22)$$

is valid. In Eq.21 and 22 the sum runs over n - total number of nodes. Moreover, the basis functions must be orthogonal,

$$\varphi_i(\mathbf{r}) \varphi_j(\mathbf{r}) = \delta_{ij} \quad (23)$$

Besides selecting an appropriate basis functions also a mesh (a grid) has to be fitted into the total volume of the simulated magnetic material. In our approach tetrahedrons represents the discretization elements with node points at each of the four vertices. On such a mesh each basis function should fulfil,

$$\varphi_i(\mathbf{r}) = \delta(\mathbf{r}_j - \mathbf{r}_i) \quad (24)$$

for all i, j nodes. If a linear basis functions were chosen, they would be sketched

in one dimension as in Fig.13. As an example, function φ_2 has a maximum at the second node and linearly goes to zero reaching it at the first and the third node. This schematic model has only four nodes, two of which (first and fourth) represents the surface boundaries.

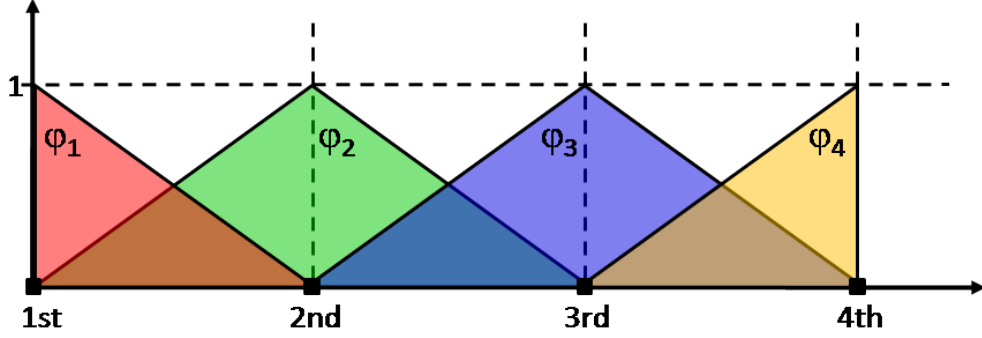


Figure 13: Global linear basis functions in one dimension for a simplified model with only four nodes.

For functional reasons, the expansion of the unknown polarisation is done stepwise: for each tetrahedron separately,

$$J^{x,y,z}(\mathbf{r}) = \sum_{\tau=1}^{N_{\tau}} J_{s,\tau} \sum_{i=1}^{N_i=4} u_{\tau,i}^{x,y,z} \varphi_{\tau,i}(\mathbf{r}), \quad (25)$$

where N_{τ} is the total number of the tetrahedrons in the region of interest and $N_i = 4$ is a number of vertices-nodes in each tetrahedron. The shape basis functions must obey the following,

$$\sum_{i=1}^{N_i=4} \varphi_{\tau,i}(\mathbf{r}) = 1 \quad (26)$$

and again,

$$\varphi_{\tau,i}(\mathbf{r}_i) = \delta(\mathbf{r}_j - \mathbf{r}_i). \quad (27)$$

Here \mathbf{r}_i and \mathbf{r}_j are the position vectors of the nodes.

One more step has to be mentioned to finalize this general overview of the Finite Element Method. In order to solve the LLG equation one has to derive an effective field at each node. This is done by integrating the expression for the total Gibbs free energy (see section 2.1.2) in each of the tetrahedron separately. Those contributions are subsequently summed up. The exchange and Zeeman terms are the functions of the magnetic polarisation. This together with Eq.21 leaves the calculated total free energy in dependence of the normalised spontaneous magnetisation ($u_i^{x,y,z}$). From

that follows equation for the effective field at each i -th node,

$$H_{i,eff}^{x,y,z} \approx -\frac{1}{m_i} \frac{\partial E_{Gibbs}}{\partial u_i^{x,y,z}}, \quad (28)$$

where m_i is the magnetic moment at the i -th node. It can be calculated according to,

$$m_i = \int_{V_i} J_s(\mathbf{r}) dV. \quad (29)$$

Here V_i is a volume of the i -th node assign in the same way as the Wigner-Seitz cell around an atom in a lattice.

A precise description of the FEM method for micromagnetics, including detailed derivations and boundary condition consideration, is enclosed in [22].

3 SEM/TEM study

3.1 Origin of the FePt films

All samples investigated in a frame of this thesis were prepared by Alexandrakis et al. in National Centre of Scientific Research Demokritos in Athens, Greece. FePt films were deposited by means of a Cooke magnetron sputtering system. A base pressure within the system was maintained at around $6.7 \mu\text{Pa}$ and argon pressure at 0.4 Pa . Firstly, 11.5 nm thick FePt layer was sputtered-deposited at $[001]$ textured MgO substrate, which was heated to 700°C . This ensured film growth in $L1_0$ phase [23]. Due to the chosen substrate texture the crystallographic orientation of FePt was expected to be with $[001]$ direction perpendicular to the film plane. It is especially possible because of a similar lattice constants of fcc MgO and fct FePt in (001) plane. Subsequently a second, graded layer was deposited while the substrate temperature was linearly decreasing. The thickness of this layer as well as the final deposition temperature were varied among the samples. In this work four most representative samples are presented and compared. Their graded layer thickness (t_{gr}), final deposition temperature (T_{final}) and cooling rate are listed in Tab.2.

Aleksandrakis et al. provided also magnetisation measurements for these samples by means of vibrating sample magnetometer. These results are shown in Fig.14 and also published in [24]. The values of the coercive field (H_c) and remanence magnetisation (M_r) are read out from this figure and additionally listed in Tab.2. All M_r were normalised to the saturation magnetisation value of a single phase FePt $L1_0$ film.

As one can see, samples A, B and C have a remanent magnetisation very similar to the one of the single phase FePt ($M_r > 0.9$). Only for the sample D M_r value is much lower and equal to 45%. It can be related to the fact, that this sample had the thickest graded layer and a final deposition temperature was much lower than 700°C . The most interesting feature visible in Fig.14 is that there is a significant difference between the coercive fields of the samples A and B. This suggests an influence of the graded layer thickness on the magnetisation properties. Moreover, such difference in H_c is also observed between samples B and C, where the thickness of the graded layer was very similar but the final deposition temperature varied by 150°C .

specimen	t_{gr} [nm]	T_{final} [°C]	Cooling rate [°C/nm]	H_c [T]	M_r [a.u.]
FePt L1 ₀	0.00	700	-	3.220	0.98
A	2.31	600	43.50	3.210	0.96
B	10.00	450	25.00	0.962	0.98
C	11.10	600	9.01	0.400	0.94
D	37.50	262	11.70	0.125	0.45

Table 2: List of the specimens analysed in this work with the characteristic parameters: thickness of the graded layer (t_{gr}), final deposition temperature (T_{final}), cooling rate of the specimen, coercive field (H_c) and remanence magnetisation (M_r) normalized to the saturation magnetisation of the FePt L1₀ film. [24]

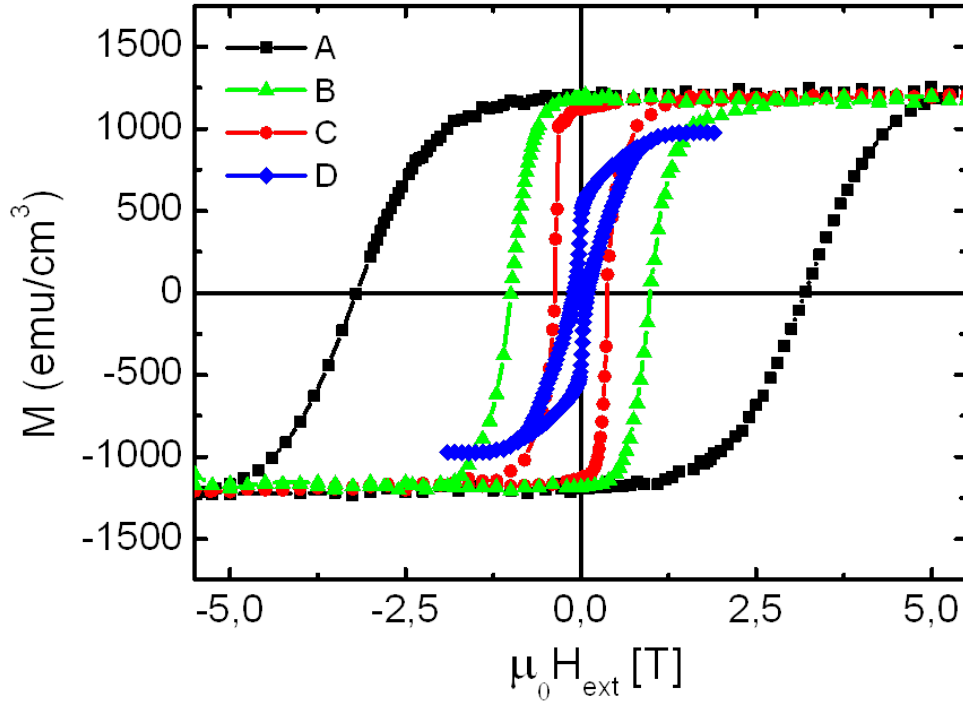


Figure 14: Hysteresis loops measured by vibrating sample magnetometer for the samples listed in Tab.2 [24]

X-ray diffraction spectra, rocking curves, AFM studies and magnetisation measurements for the samples very similar to the one presented in this work are published in [7]. This paper, however, does not answer the following questions: how the nanostructure of the FePt films look like and how it is influenced by the varied deposition conditions. Such analysis will be presented in the subsection *Results and discussion* of this chapter.

3.2 TEM sample preparation

All the samples were prepared for a TEM plain view (PV) and a cross section view (CSV). Mostly a manual preparation method was applied. If, however, only a small amount of the material was available, Focus Ion Beam (FIB) device was used. It is more precise sample preparation method but also more expensive.

The samples in the manual method were initially cut by a wire saw into 3 mm x 3 mm pieces for PV specimens and 3 mm x 1.5 mm for CSV. In case of CSV two such elements were glued together film-to-film with M-bond 610. This is done in order to obtain a wider area for an investigation. A polishing was done by means of MetPrep4 Grinding/Polishing machine with Powerhead4. Diamond sheets with grit: 6 μm , and subsequently 3 μm and 1 μm were used to obtain a final specimen thickness of about 10 μm . Samples were glued to the copper rings with outer diameter of 3mm as shown in Fig.15. These copper rings are especially suited for the TEM sample holder.

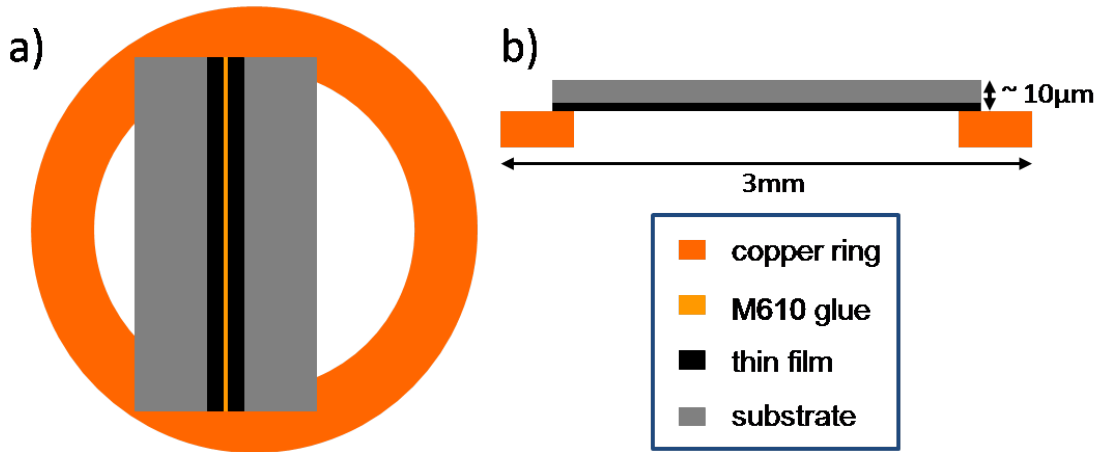


Figure 15: A) Positioning of the cross section view specimen on the copper ring. B) A profile of the plane view specimen on the copper ring.

After the manual polishing and thinning a Precise Ion Polishing System (PIPS) was used in order to obtain areas in the region of interest with thickness of only a few hundreds of nanometers. This allows the electron beam in TEM to pass through. PIPS involves bombarding the specimen with Argon ions, which sputter out the material. During operation a pressure of around 0.1 Pa was maintained, whereas the base pressure was $7 \cdot 10^{-4}$ Pa. The milling was done in steps, in which the acceleration voltage of the Argon ions was gradually decreased from 3 keV to 1 keV. The total time of the polishing varied between 5 to 15 hours, depending on the initial thickness of the specimen and its type (PV and CSV). Usually the plain view specimens required longer sputtering times. At the end of PIPS procedure small holes in the sample were visible, around which the material was sufficiently

thin for the TEM analysis.

If a limited amount of material did not allowed to risk the manual polishing FEI Quanta 200 3D Dual Beam FIB device was used for CSV preparation. In a FIB vacuum chamber a very thin slice of the material was cut with a beam of energetic Gallium ions (5 kV to 30 kV). The beam current between 1 pA and 30 nA was applied. Subsequently, the cut membrane was attached to the extraction needle and manipulated into a TEM copper lift-out grid (Fig.16.A). The slice was micro-welded to the grid using FIB tungsten deposition [25]. Scanning Electron Microscope (SEM) images of the prepared specimen inside the FIB chamber are presented in Fig.16.B and C. In the thinnest region the sample was about 161.89 nm thick, which provided a good visibility in TEM.

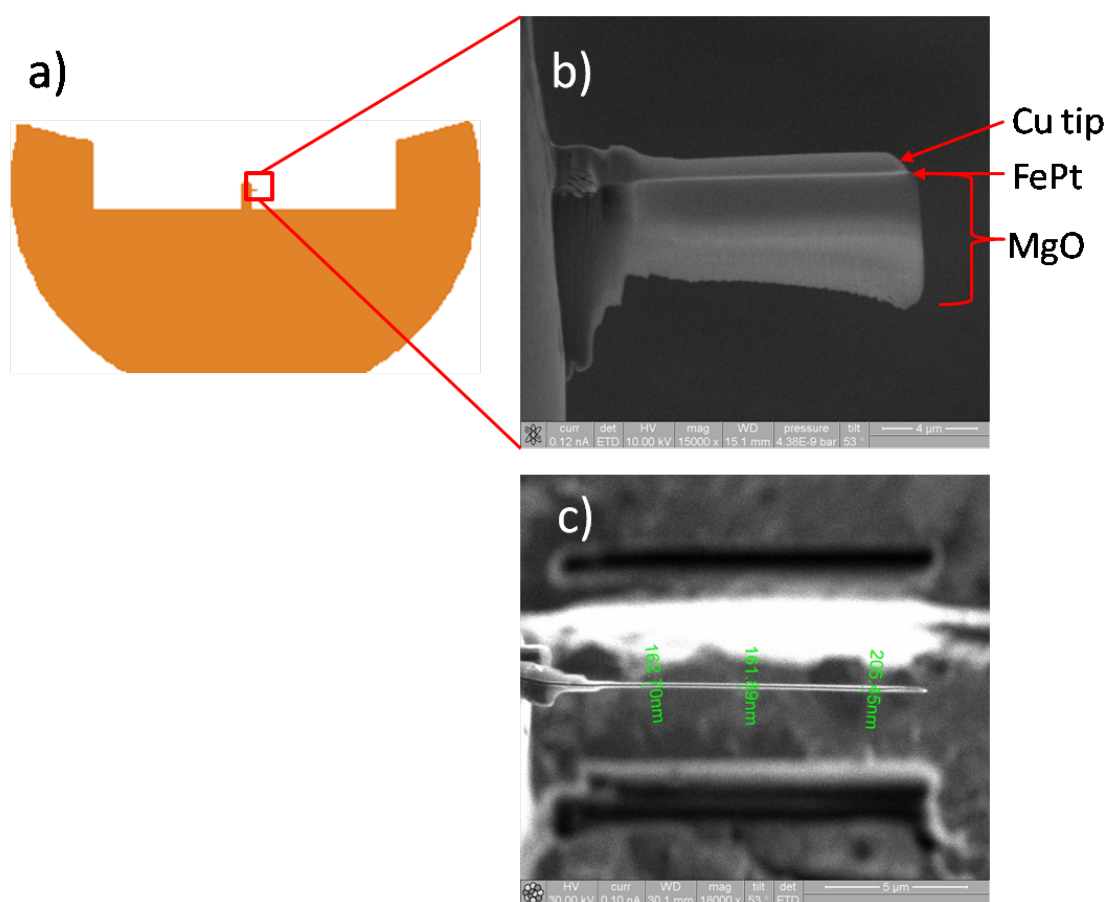


Figure 16: A) Schematic drawing of the TEM copper lift-out grid with the small tip (in the red square) at which the sample is welded. B) SEM image of the tip with the attached sample. C) Profile SEM view of the tip with the indicated sample thickness.

In order to remove contaminations such as carbon and oxides the specimens were plasma cleaned directly before the investigation. This was done independently from the type of the sample preparation. More precise description of the manual preparation can be found in [26].

3.3 Results and discussion

Before TEM sample preparation procedures all specimens were investigated with Scanning Electron Microscope (SEM) and Energy Dispersive X-ray (EDX) analyser. FEI Quanta 200 Field Emission Gun SEM (FEGSEM) with EDAX Pegasus XM4 was utilized. Plain views for all four specimens obtained with 50000x magnification are presented in Fig.17. Particular images are denoted by the specimen letter (A, B, C, D see Tab.2). An electron acceleration voltage and pressure in the SEM chamber are given below the images.

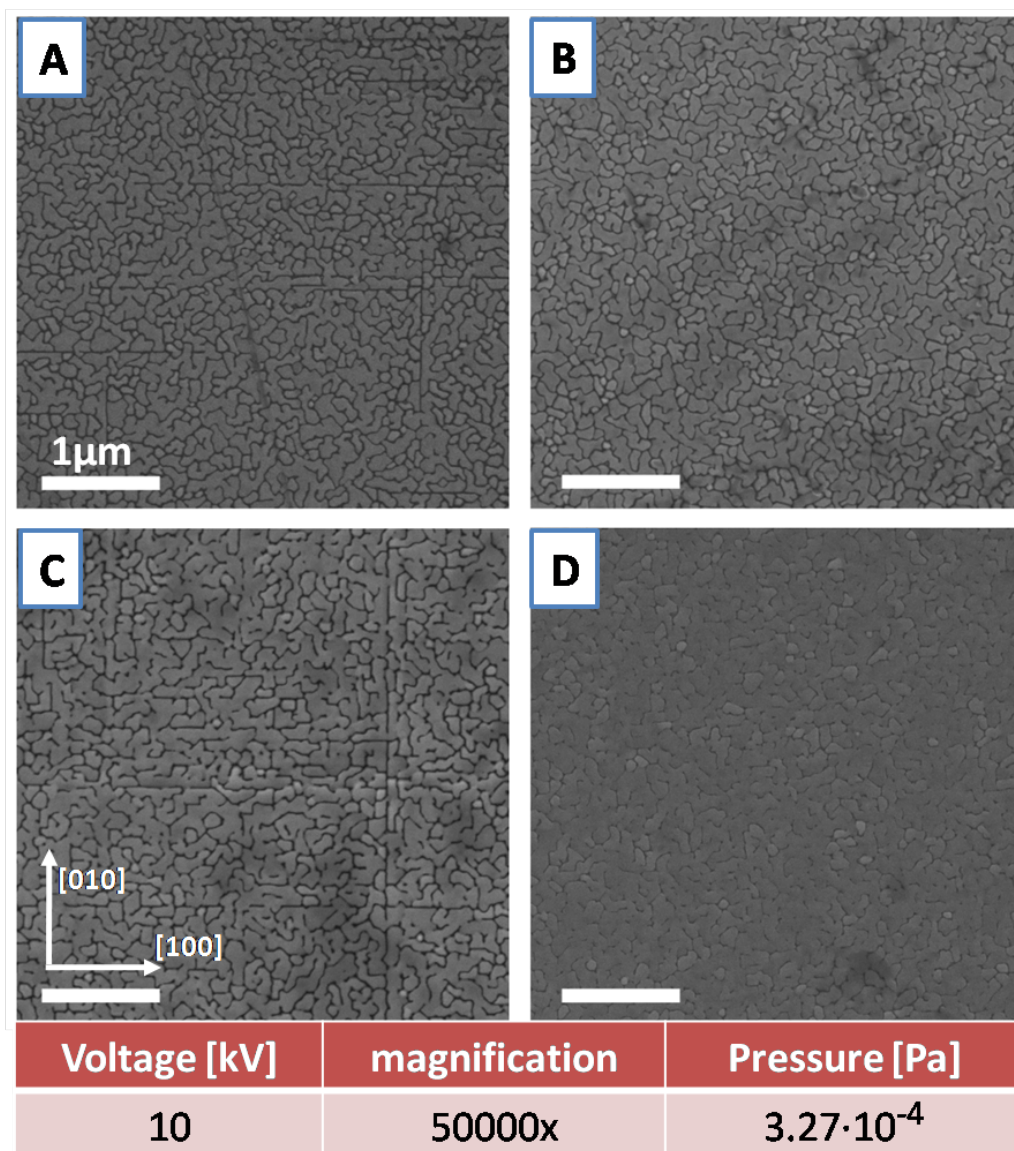


Figure 17: SEM plain views for all four specimens (A,B,C,D - as in Tab.2). All scale bars have a length of $1 \mu\text{m}$. An electron acceleration voltage, magnification and pressure in the SEM chamber are given below the images. Additionally, lattice directions are marked on sample C.

All samples are characterized by a complicated granular structure. Grains have irregular shapes and variable sizes. Grain boundaries for samples A, B and C are clearly distinguishable, whereas in case of much thicker specimen D they are much narrower and partially merged. In samples A and C partial alignment of the grain boundaries along [100] and [010] directions is visible. This ordering is possible because of a relatively high final deposition temperature for both specimens (600 °C). When T_{final} was lower, as for sample B (450 °C), the grain boundaries alignment is no longer visible. Additionally EDX surface analysis was made before the destructive TEM sample preparation. Spectra for all samples were very similar. One representative example for specimen B is given in Fig.18. On the top of the background exclusively Fe and Pt peaks are recognisable proving the expected elemental composition of the samples.

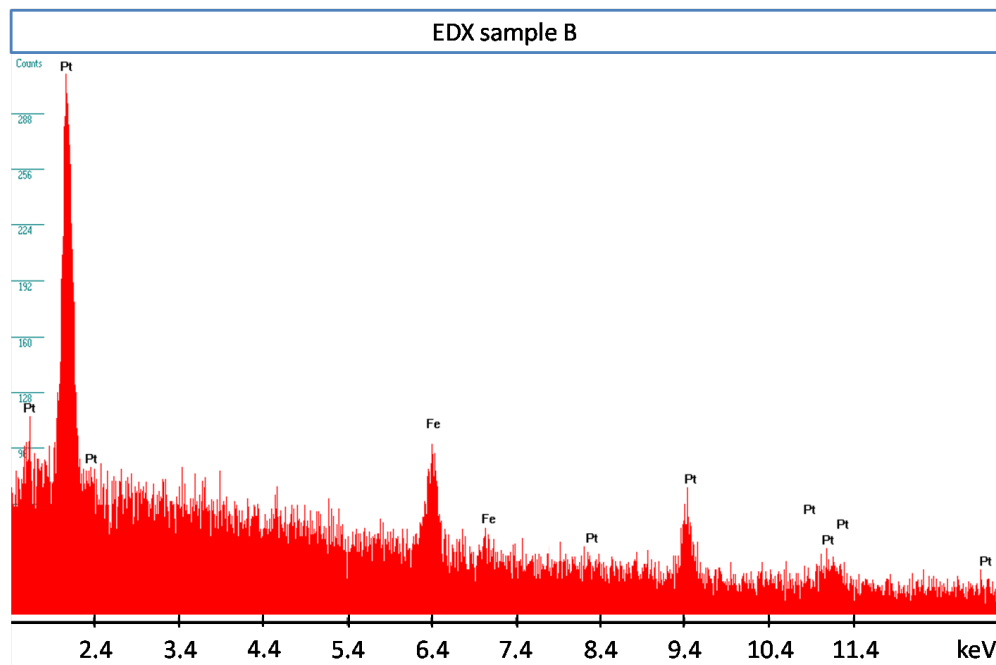


Figure 18: A representative EDX spectrum for sample B. Elemental composition of the film surface was proven to be FePt.

After TEM sample preparation plain view Bright Field (BF) and Dark Field (DF) images were recorded as well as Diffraction Patterns (DP). This set of results for sample B is presented in Fig.19. Other specimens are omitted since the main structural differences were already pointed out in Fig.17. Sample B was chosen as representative, because obtained images were of the best quality. Recorded diffraction pattern is characteristic for a double diffraction: single DP spots are split into several spots (see chapter 2.4.2). Red circles mark the dots corresponding to the MgO and FePt planes, whereas blue circles show the aperture selections for the dark field imaging.

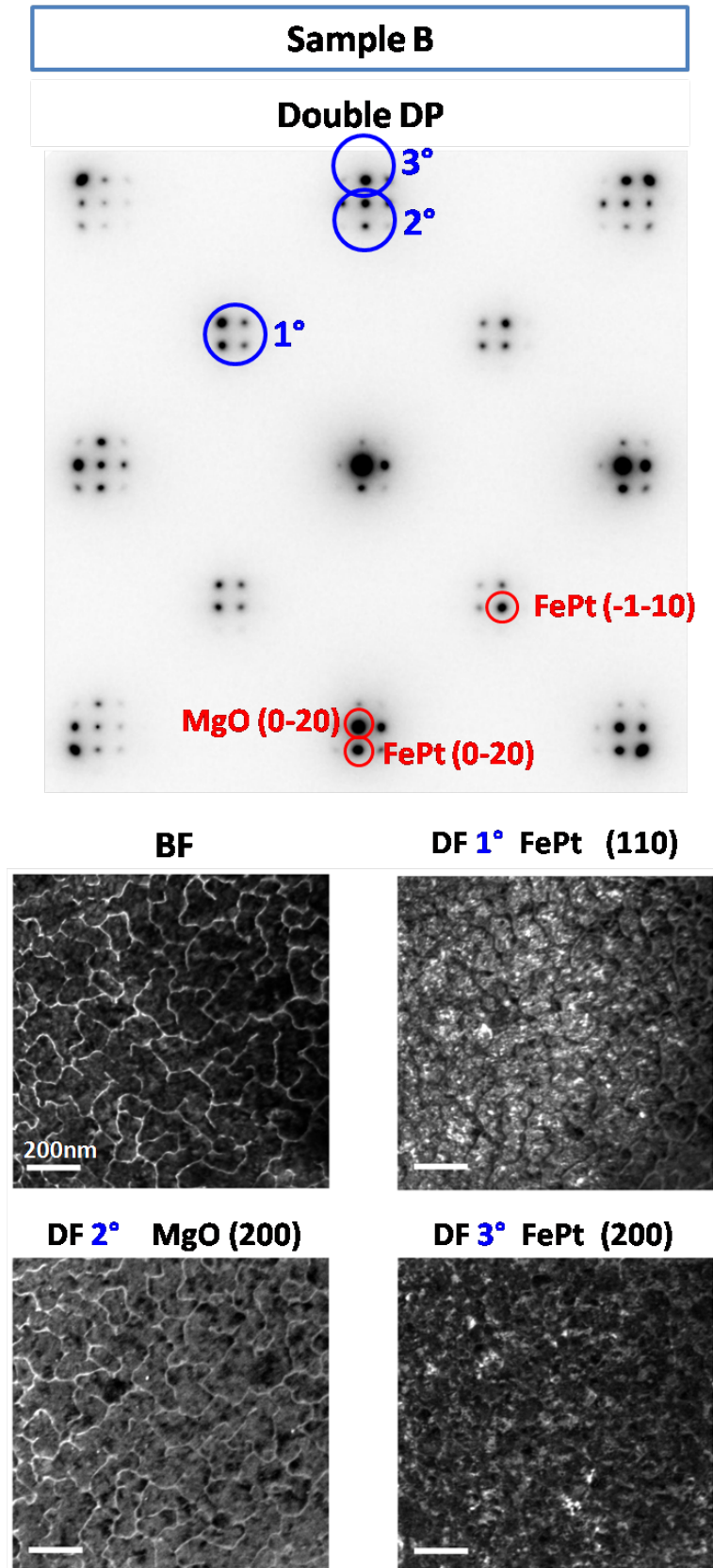


Figure 19: TEM plain view results for sample B: double diffraction pattern (DP), bright field image (BF) and three dark field images (DF) taken from DP spots marked by blue circles. All scale bars have a length of 200 nm. Spots with recognised material (MgO or FePt) and crystallographic planes (Miller indices) are marked in DP with red circles.

In the DF 1° image grain volumes are bright, whereas boundaries stay dark. For such aperture position only spots corresponding to FePt in (110) plane are selected. In DF 2° only dots representing MgO are chosen, hence spacings between the grains, where the substrate is visible, are highlighted. For this plane view much less of FePt was found in (200) planar orientation (DF 3°) than in (110)(DF 1°).

More quantitative information concerning crystallographic and chemical structure of the investigated material can be obtained from the cross section views. In Fig.20 a wide CSV overview for all samples is presented. The specimen elements (film, glue, grid) are indicated directly in the images. Exclusively in Fig.20.B the copper grid is visible since this sample was prepared by FIB. One can notice that the thickness of the film is more uniform in samples B and D than in A and C. Moreover, in cases A and C the intergrain spacings appear to be bigger and they reach down to the substrate. This agrees well with the features observed for the same specimens in Fig.17: the grain boundaries for these specimens are more distinct.

Directly from this images average thickness of the FePt layer was measured and compared with the calculated values (from magnetron sputtering deposition rate). A summary of these quantities is given in Tab.3. All the films are thicker than expected, hence the deposition rate was higher than the one assumed.

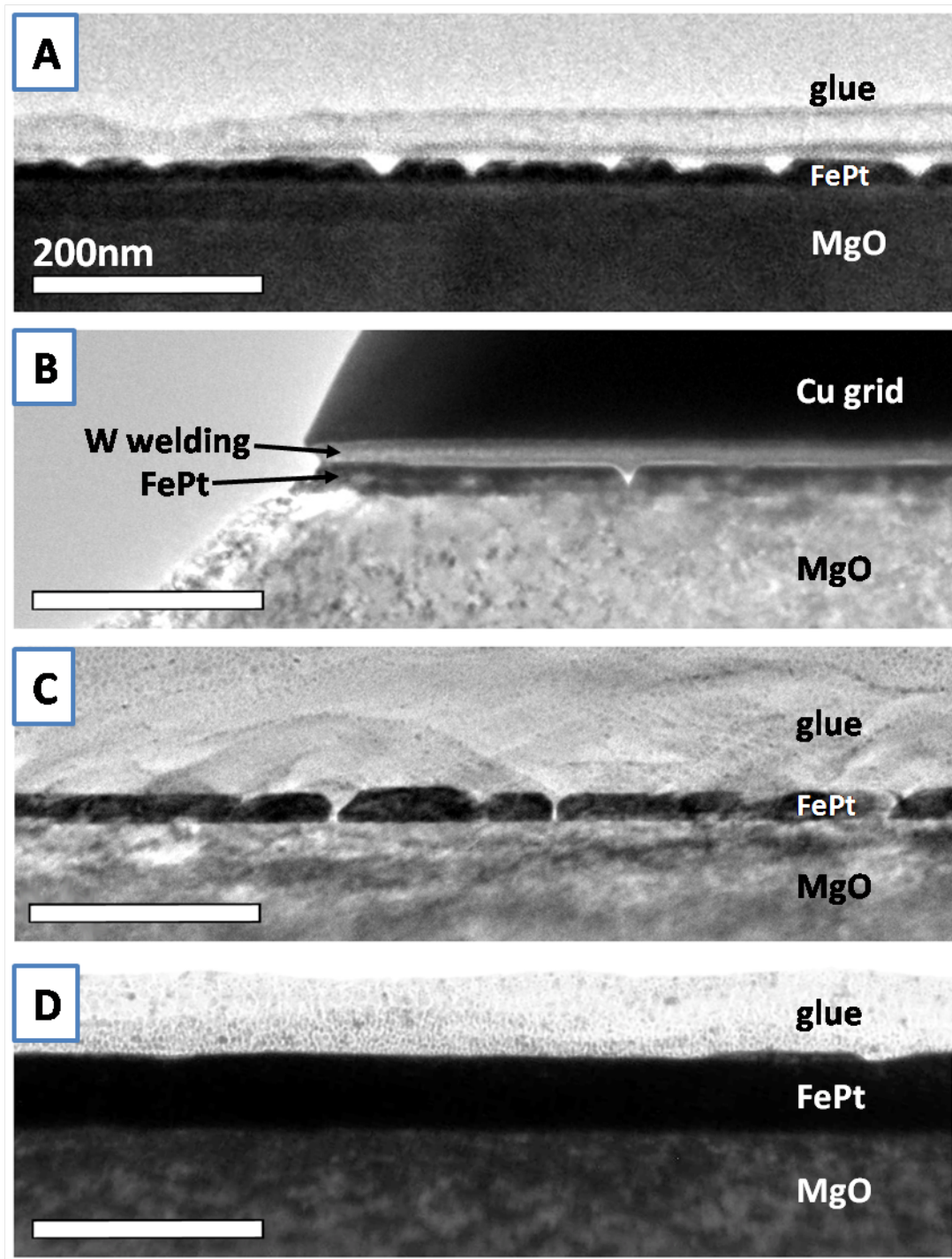


Figure 20: Bright field cross section views for all specimens. Structural elements: Cu grid, glue, W welding, FePt and MgO are marked directly at the images. All scale bars are 200 nm long.

specimen	expected thickness [nm]	measured thickness [nm]
A	13.31	20
B	21.00	28
C	22.10	28
D	48.50	60

Table 3: A summary of the expected specimen thickness (calculated from the magnetron sputtering rate) and the one measured from the cross section views.

The goal of the magnetron sputtering was to obtain FePt films with defined thickness and chemical composition (50% of Fe and 50% of Pt). Since the thicknesses differed from the one expected, the chemical compositions were as well reviewed. Chemical EDX analysis for CSV specimens allows not only to record surface information, as in SEM, but also to study chemical composition along the film thickness with nanometer resolution.

An example of the obtained spectrum for sample B is presented in Fig.21. This CSV specimen was prepared by means of FIB. In the inset a bright field TEM image of the specimen is showed as well as a STEM image with a marked red spot from where the spectrum was recorded. Elements originating from the film (Fe,Pt) are clearly recognisable. Additionally, tungsten (W) and gallium (Ga) peaks have a high nr of counts. Both elements are remnants after the FIB procedures (see chapter 3.2). Also substrate elements, magnesium and oxygen, are visible. The last recognised element is copper (Cu), which originates from the lift-out grid.

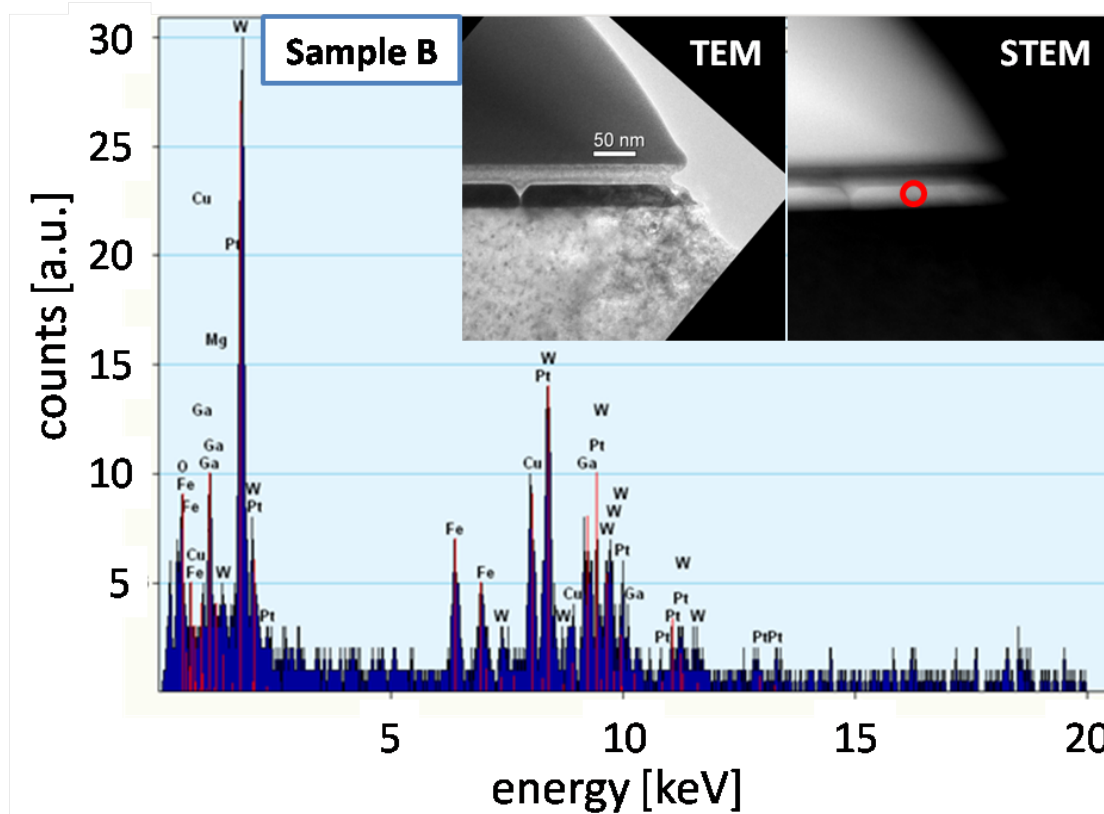


Figure 21: An example of the EDX spectrum for sample B. In the inset TEM and STEM CSV images are shown. In the STEM picture red circle marks the area from which the spectrum was recorded.

Subsequently, a line EDX scans were recorded. Each scan covered length of 40 nm. Spectra were registered in 2 nm step size. In Fig.22 two such elemental profiles are shown and their positions are marked in the STEM image. Signals from the High-Angle Annual Dark Field (HAADF) detector are presented in the uppermost diagrams. They present intensity profiles along the lines 1° and 2°. The HAADF detector is highly sensitive to atomic number variations (so called Z-contrast). The Z-contrast is also recognisable in the STEM figure. Therefore, the strongest signal corresponds to the areas with heaviest element: Pt. A layer of W between the film and the copper grid is very thin, hence it is less bright. Thick Co grid gives strong signal. Material with the lightest elements, MgO, appears as the darkest.

Analysing the elemental profiles shown below HAADF diagram one can notice a diffusion of Mg into the film from the left side and W from the right side. Most probably they were deposited at the FePt layer by Ga ions during FIB procedures. Oxygen does not follow similar curve as magnesium. It is possible, that as a volatile element it evaporated when removed from the substrate. Also Cu from the grid and Ga from ion FIB beam are recognised. Undesirably, both of the elements were deposited at the top of the film.

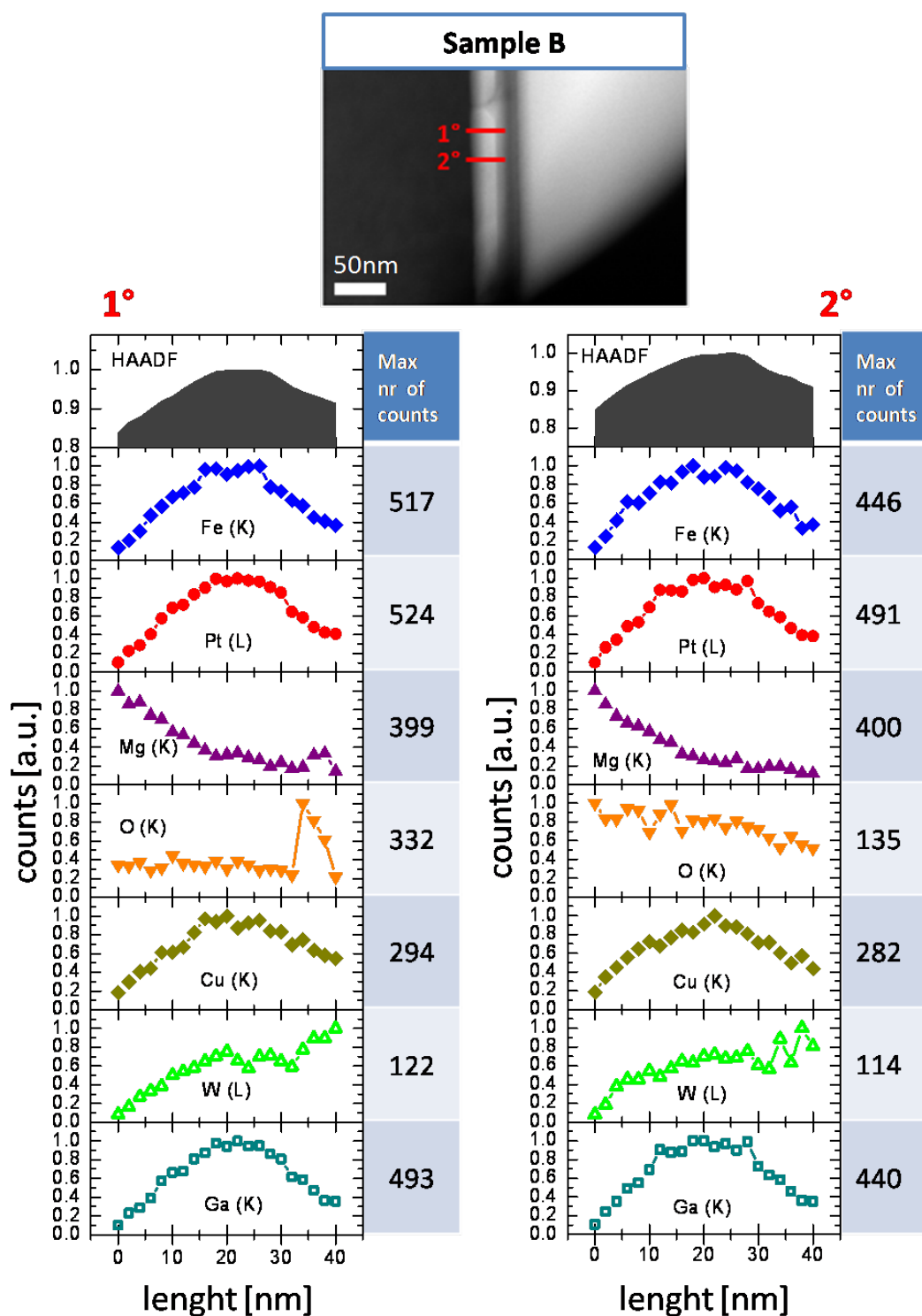


Figure 22: EDX line profiles along the film thickness of sample B. Spectra were recorded in 2 nm step size along the distance of 40 nm. The profile tracks (1° and 2°) are marked in the STEM image at the top of the figure. All curves are normalised to the maximal number of counts, given in the column on the diagram right side. In the brackets, next to the element name, electron shell is given from which the signal was obtained. The upper most diagrams represent High-Angle Annual Dark Field (HAADF) detector signal.

The most important profiles are of Fe and Pt. They have the highest maximal number of counts and maxima of their profiles lie approximately in the centre of the film. Moreover, they are very similar, which suggests that the chemical composition along the film thickness does not vary. A proof, that the film is made of Fe_aPt_b with $a = b$ is given in Fig.23. A ratio between iron and platinum EDX counts is plotted along the line profiles. For both cases, 1° and 2° , this ratio oscillates around one. EDX data of other specimens showed very similar features giving the same average Fe/Pt ratio, hence these results are omitted.

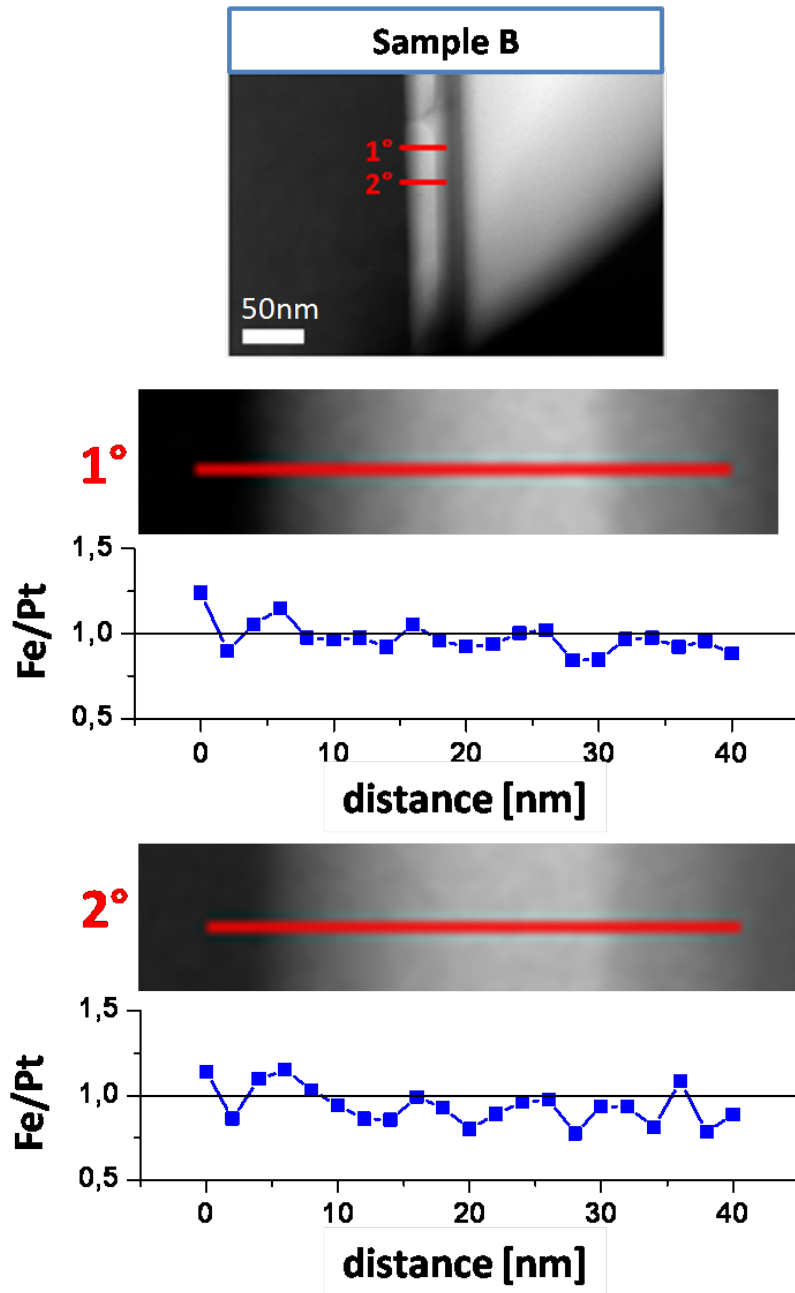


Figure 23: Diagrams with Fe/Pt ratios of the EDX counts calculated along the line scan marked in the STEM images by the red lines.

After checking the chemical composition of the films a detailed high resolution crystallographic analysis was carried out. Again sample B was taken as an example, since the FIB preparation allowed to take good quality images. In Fig.24 cross section views are presented with three different magnifications. Blue rectangles mark the zooming areas. As a region of interest the thinnest non-damaged film part was chosen at the edge of the lift-out grid tip. In the highest obtained magnification (Fig.24 c)) a periodicity of the crystallographic planes is recognisable. Most of the film volume has a two-fold symmetry (as in the 2° square). Only at the top of FePt, similarly as in the whole MgO substrate, a four-fold symmetry occurs (as in the 1° square). This is already recognisable with the naked eye, however in order to read out the lattice parameters a Fast Fourier Transform (FFT) was done. The areas for which FFT was calculated are marked by the red squares in Fig.24 c) and obtained images one can find on the right side of this figure. In case 1° the reciprocal length marked by red arrows equals after inversion 1.88 \AA . This agrees with the simulated distance between the $\{002\}$ planes of FePt A1, which is 1.91 \AA (see Tab.1). In case 2° the value calculated from FFT amounts 3.76 \AA , which is close to $[001]$ lattice constant of FePt L1₀; 3.71 \AA (Tab.1).

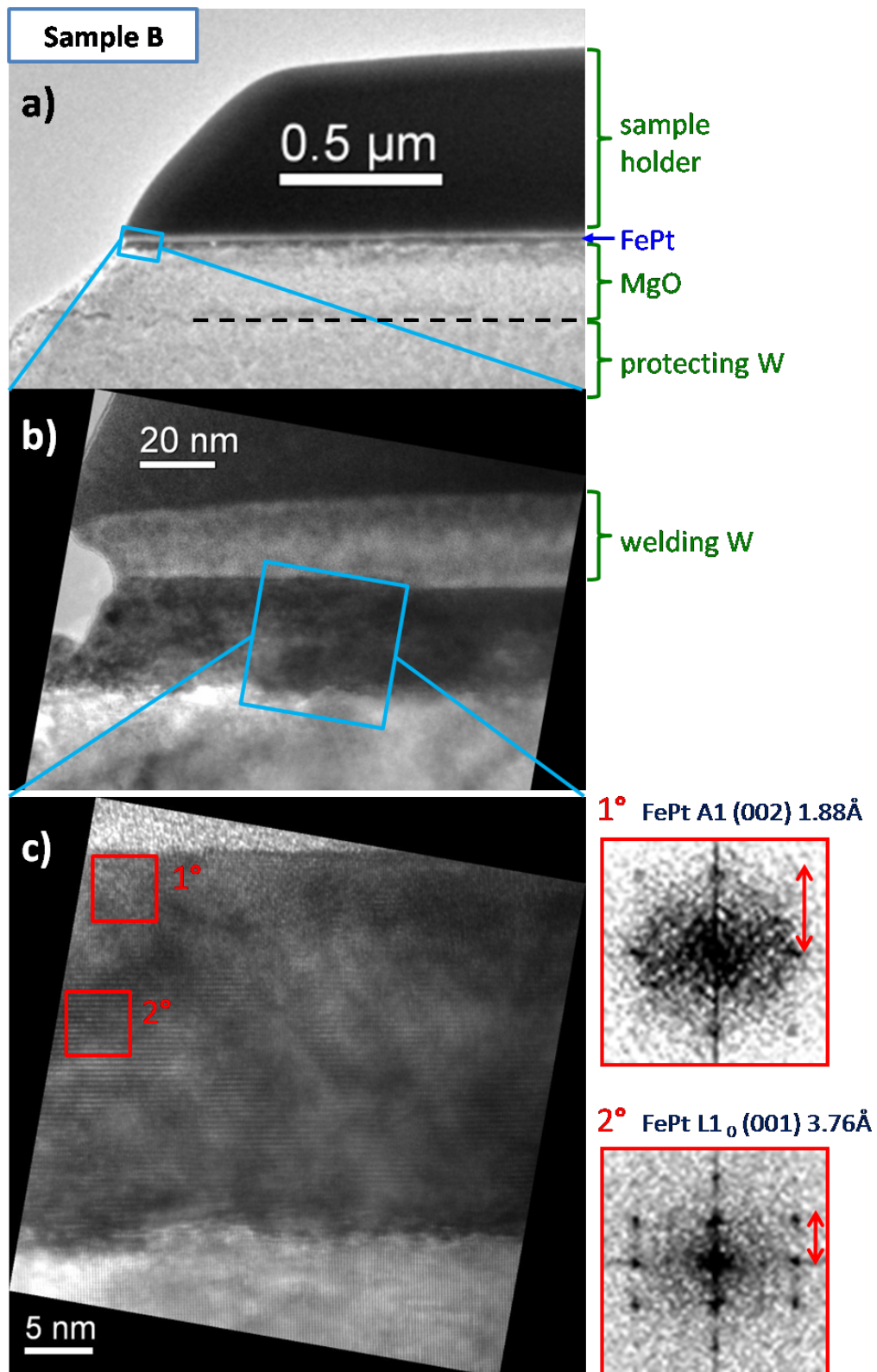


Figure 24: TEM bright field images of the cross section views for sample B. The blue rectangles mark the zooming areas. In figure c) the red squares denote the region from which the Fast Fourier Transform (FFT) was calculated. FFT images are shown on the left side of the figure c). Measured lattice constants and corresponding FePt structures are written above each FFT picture.

In order to inspect the distribution of both FePt phases (A1 and L₁₀) in a wider area of the film diffraction pattern and dark field images were recorded. Saved results are demonstrated in Fig.25. In the diffraction pattern a characteristic superposition of DP spots originating from MgO and both phases of FePt is visible. This agrees very well with simulated SADP (Fig.9, section 2.4.2). In the first dark field image (DF 1°) an aperture was centred around two DP spots, which lie so close to each other that separating them would not be possible. They correspond to FePt L₁₀ and A1 phase in (002) plane. As one can see, bright areas are distributed in the whole film volume. For the spot nr 2° only substrate is bright. Additionally, if one compare DF 1° and 3° it is clear that the L₁₀ phase does not occur in the total volume of the film. At the top of the material a stripe of only A1 phase occur, which is less than 10 nm thick. The A1/L₁₀ interphase appears in this magnification to be more or less flat.

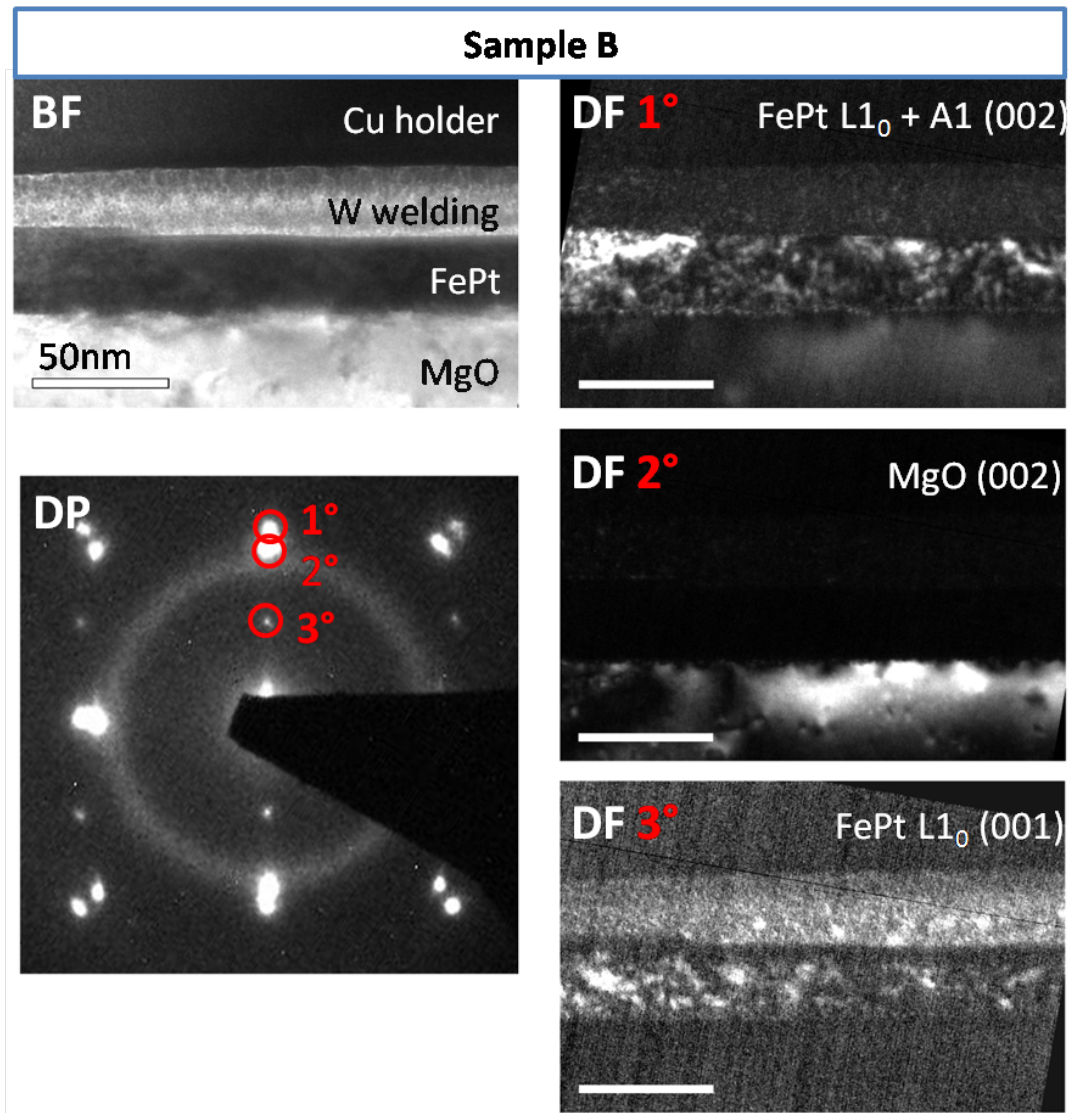


Figure 25: A set of TEM CSV results for sample B: Bright Field (BF) and three Dark Field (DF) images, as well as Diffraction Pattern (DP). Scale bars in all images correspond to 50 nm. In DP red circles mark the aperture selection for DF imaging. Materials, phases and lattice planes, which are highlighted are written in the top right corner of the DF pictures.

For a comparison also diffraction pattern and dark field images are analysed for sample C. The results are summarised in Fig.26. This time spots of FePt L₁₀ (-20-1) and FePt L₁₀ + A1 (-20-2) were chosen for the DF imaging. Two sets of images are presented: a wider overview (BF, DF 1°, DF 2°) and a selected grain (BF, DF2 1°, DF2 2°), for which it was easy to recognise and localise the two FePt phases. The difference between DF images taken from the spot 1° and 2° is, that in the L₁₀ + A1 pictures a narrow stripe at the top of the film is strongly highlighted. This is not the case for DF 1° and DF2 1°. Hence again material in A1 phase occur at the top of the film.

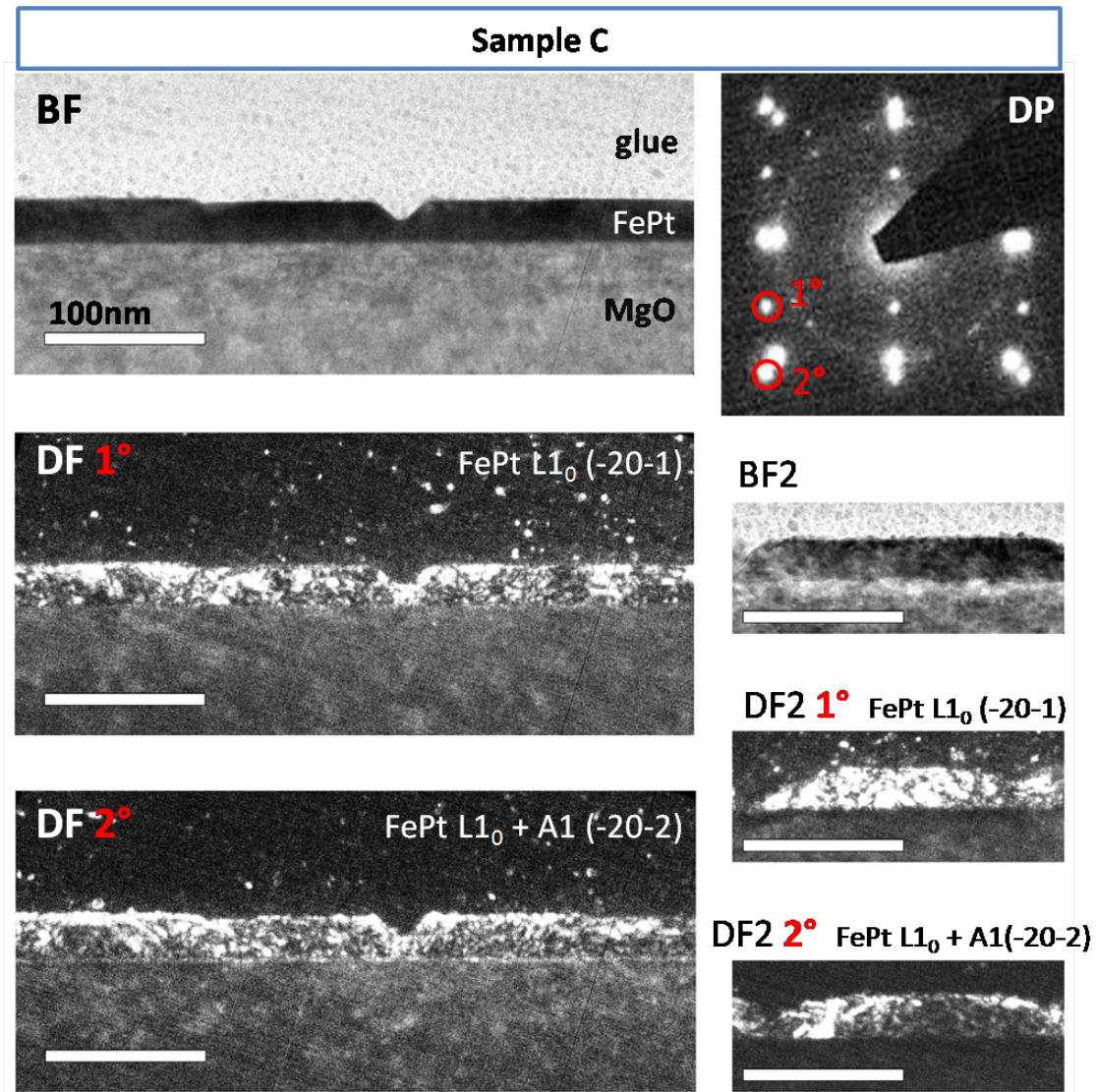


Figure 26: A set of TEM CSV results for sample C: Bright Field (BF) and Dark Field (DF) images, as well as Diffraction Pattern (DP). Scale bars in all images correspond to 50 nm. In DP red circles mark the aperture selection for DF imaging. Materials, phases and crystallographic planes, which are highlighted are written in the top right corner or above the DF pictures.

Based on Fig.25 and 26 it is difficult to judge how exactly the A1/L1₀ interphase look like. A detailed HRTEM analysis together with FFT calculations was carried out for all specimens. As an outcome it was possible to guide a line at the border between the two FePt phases in high magnification images. The best obtained results are presented in Fig.27. Sample A with the thinnest "graded" layer and final deposition temperature of 600°C (t_{gr} and T_{final} in Tab.2) has a perfectly flat interface. Sample B with a thicker t_{gr} (10 nm) has more irregular interphase, but not as much as sample C with a similar t_{gr} (11 nm). Since what mostly varies between sample B and C is the final deposition temperature (450°C and 600°C respectively),

the cooling rate is the parameter which influences the interphase roughness. Sample D, which is the thickest, has similar cooling rate as sample C ($11.70^{\circ}\text{C}/\text{nm}$ and $9.01^{\circ}\text{C}/\text{nm}$ respectively) and the roughest interphase. For instance, one can notice a single inclusion of $L1_0$ phase embedded in an A1 surrounding. Summarising, both: the thickness and the cooling rate were the parameters influencing the interphase roughness.

In all cases no intermediate phases between A1 and $L1_0$ were found. Alexandrakis et al. in his paper expected rather a gradual changes from one to the other phase [7], however here it is not the case. This is also why chosen by him expression: "graded layer", t_{gr} does not properly describe the problem.

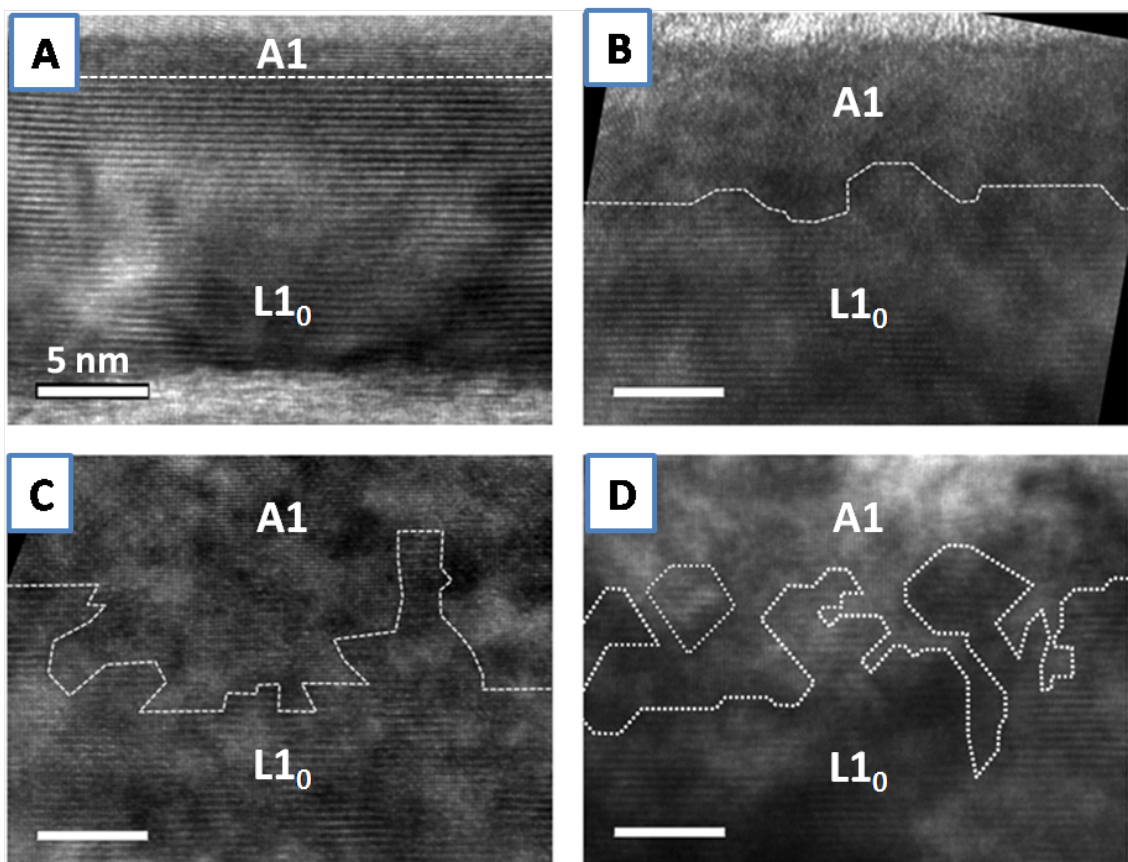


Figure 27: High Resolution TEM cross section views of all investigated specimens. Recognised two FePt phases (A1 and $L1_0$) are marked in the images and their interphase is symbolised by the white dashed line. All scale bars are 5 nm long.

4 Micromagnetic study

In this chapter magnetic properties of the exchange spring media are considered. The rough interphase, found in the FePt TEM analysis, between magnetically hard and soft material is analysed in details. A Finite Element Micromagnetic simulations are done in order to determine nucleation, pinning and switching fields of the media. The discussion starts with a derivation of the pinning field for exchange spring films (section 4.1). This formula is subsequently used for a comparison with the simulation outcomes, which are presented in section 4.3. A detailed description how the experimental results were transferred into micromagnetic models is presented in 4.2 Nanomagnetic modeling.

4.1 Derivation of the pinning field

The pinning field of a domain wall in a material with gradually changing anisotropy constant ($K_1(z)$) along the thickness of the medium (z -direction) was already proposed by Süss [6],

$$H_P(z) = \frac{2}{J_S} \frac{\partial \sqrt{AK_1(z)}}{\partial z}, \quad (30)$$

where J_S is the saturation polarisation and A is the exchange constant of the medium. This equation is only valid if $J_S = const.$ If one considers FePt L1₀/A1 as an example, the saturation polarisation of L1₀ and A1 phase is not the same, hence equation (30) is no longer valid. Taking this fact into account one can derive an appropriate formula for the pinning field.

A simple model with the domain wall at a given position z and applied external field H is shown in Fig.28.

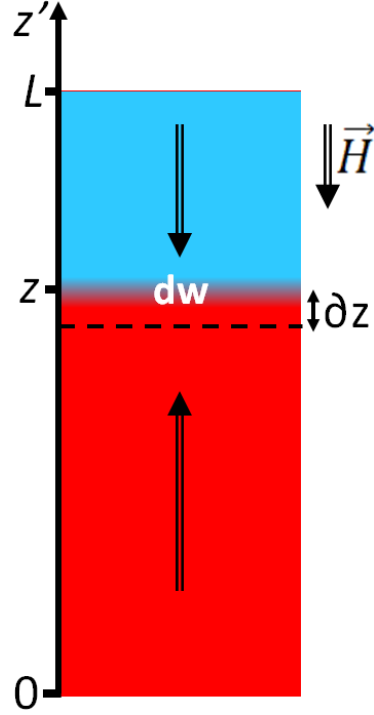


Figure 28: A simple model during the reversal process with the domain wall (dw), which is moved by the external field \mathbf{H} from position z to $z - \partial z$. The directions of the partial magnetisations and the external field are given by arrows.

The total magnetic free energy of this system per unit area in xy -plane is given by

$$E_{tot} = E_{DW}(z) + \int_0^z J_S(z')H dz' - \int_z^L J_S(z')H dz', \quad (31)$$

where E_{DW} denotes an energy (per surface unit) of the domain wall. The two integrals correspond to the Zeeman terms for the magnetisation pointing up and down respectively. The magnetostatic energy is neglected in this approach. The domain wall can now move from z to $z - \partial z$ for a given H only if $\partial E_{tot}/\partial z = 0$, which leads to

$$\frac{\partial E_{DW}(z)}{\partial z} + H \frac{\partial}{\partial z} \left[\int_0^z J_S(z') dz' + \int_L^z J_S(z') dz' \right] = 0. \quad (32)$$

Using the First Fundamental Theorem of Calculus,

$$\frac{\partial}{\partial z} \left[\int_{const}^z g(z') dz' \right] = g(z), \quad (33)$$

one obtains

$$\begin{aligned} \frac{\partial E_{DW}(z)}{\partial z} + 2J_S(z)H &= 0 \\ H &= -\frac{1}{2J_S(z)} \frac{\partial E_{DW}(z)}{\partial z}. \end{aligned} \quad (34)$$

If one assumes a perfect Bloch domain wall and $K_2 = 0$, its the energy density can be expressed by $E_{DW} = 4\sqrt{AK_1(z)}$. Moreover, it is theoretically proved, that the exchange stiffness constant A hardly depends on the chemical order of FePt [27], hence one can assume that it is the same for L1₀ and A1 phase. With these approximations one arrives at the final expression for the pinning field as a function of position z ,

$$H_P = -\frac{2}{J_S(z)} \frac{\partial \sqrt{AK_1(z)}}{\partial z} = -\frac{\sqrt{A}}{J_S(z)\sqrt{K_1(z)}} \frac{\partial K_1(z)}{\partial z}. \quad (35)$$

Equations (35) and (30) are consistent if $J_S = \text{const}$. The negative sign comes from the different direction of the external field. From this formula one can easily anticipate the switching field H_{sw} of the media with known distributions of J_S and K_1 ,

$$H_{sw} = \max(H_P(z)). \quad (36)$$

This is, however, only valid when the nucleation field is smaller than the pinning field.

In order to confirm the validity of the above derived equation a test Finite Element (FE) micromagnetic simulation was performed for a model with dimensions of 1 nm x 1 nm x 100 nm (Fig.29 right). This cuboid was a stack of cubes with an edge length equal to 1 nm. To each cube material parameters were assigned according to

$$\begin{aligned} K_1(z) &= 5 \cdot 10^6 \cdot \left(1 - \frac{z}{100}\right)^3 \left[\frac{\text{J}}{\text{m}^3}\right], \\ J(z) &= 1.58 - 0.58 \frac{z}{100} [\text{T}], \\ A &= \text{const} = 10^{-11} \left[\frac{\text{J}}{\text{m}}\right], \end{aligned} \quad (37)$$

where z -value was always chosen at the center of the respective cube. The dependency of $K_1 \sim -z^3$ and $J \sim -z$ are chosen arbitrarily in order to show universality of the derived equation. It is only assured, that the nucleation field is smaller than the maximal pinning field of the model. The values of $K_1(z)$ and $J(z)$ at $z = 0$ correspond to the FePt L1₀ phase and at $z = 100$ to the FePt A1 phase. Moreover, the one dimensional approach in the pinning field derivation was taken into account, thus the test model was much longer in z -direction (100 nm) than in

x,y-direction (1nm). For such models the best agreement between the analytical and numerical approach was expected.

Figure 29 presents the comparison between the magnetisation curve obtained from the test simulation and the analytically calculated pinning field using Eq.(37). For the external field values between 0 and -0.1 T the reversal of the grain is described by the nucleation process, hence there is no agreement between the simulation and the analytical approach. At about -0.1 T, however, the pinning field starts to dominate the switching mechanism of the model. From this point forward both curves are close to each other and have similar slopes. The difference in the coercive field is of about 0.013 T. This proves that Eq.(35) is a good approximation for the pinning field.

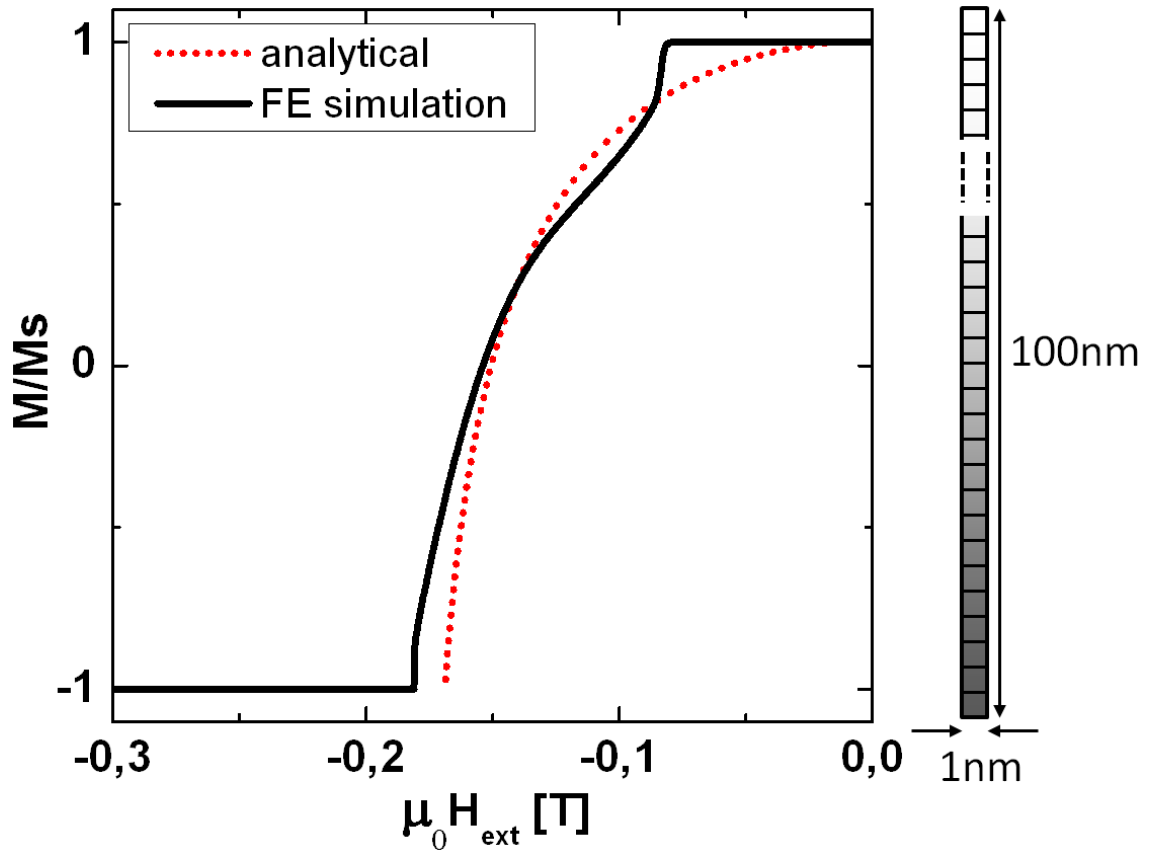


Figure 29: Left: A comparison between the magnetisation curve obtained by the micromagnetic simulation and the pinning field given by the analytical equation derived in this paper. Right: a schematic drawing of the FE model used in the simulation with cubic discretization cells. The color gradient symbolize the gradually changing magntocrystalline anisotropy and saturation polarisation.

4.2 Nanomagnetic modelling

From the high resolution images of the FePt L1₀/A1 media presented in Fig.30 the L1₀ distributions were calculated as following: Horizontal lines were drawn in these images every 1 nm. Then it was measured how much of a given line lies within the hard phase. This length was divided by the total length of the image giving the ratio with arbitrary units.

For the sample with the smoothest transition from L1₀ to A1 (Fig.30A) the hard phase distribution can be fitted in the interphase region by a linear or, better, by a logistic function. In the case of Fig.30B a quadratic fitting function is appropriate. The yellow square in the HRTEM image represents the chosen discretization element used for numerical models: The smallest cells to which the material parameters of hard or soft phase can be assigned are cubes with a side length 1 nm. When it comes to Fig.30C, the L1₀ distribution in the variation region has to be described by a piecewise analytical function, thus it is left without fitting. In this figure worth noticing is the irregularly shaped obstacle of the hard phase, which is not connected with the rest of the L1₀ phase.

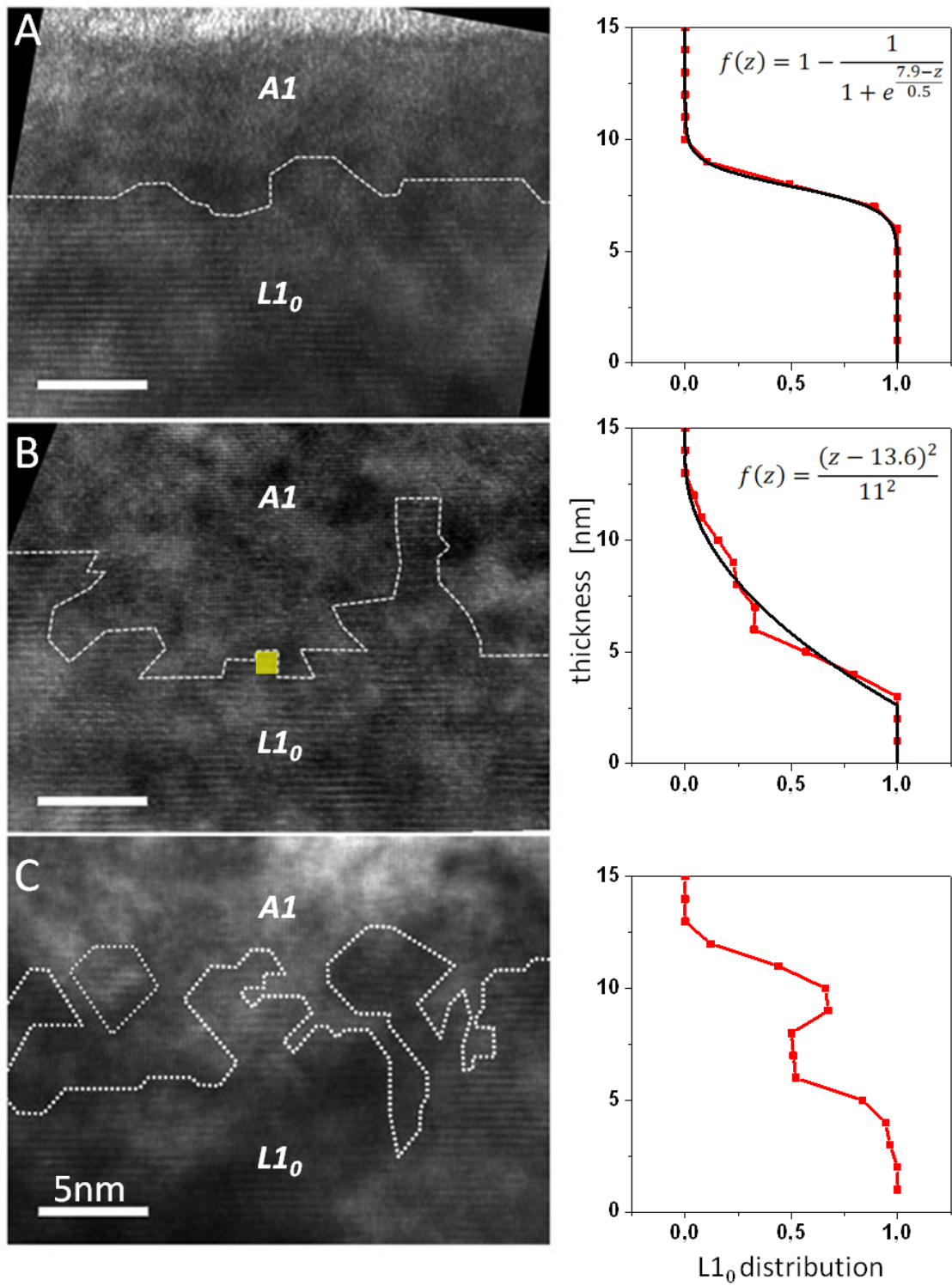


Figure 30: Left: HRTEM images of the FePt L1₀/A1 media [24]. Right: the corresponding L1₀ distributions along the thickness of the samples (red dotted lines). For the cases A and B additionally analytical fitting curves are plotted (black lines) and their formulas are given.

Based on these experimental observations, three types of Finite Element (FE) models were created for the micromagnetic simulations:

1. In the first type the models have the shape of a square cuboid with $10 \times 10 \text{ nm}^2$ base and 25 nm height (Fig.31.A). These are realistic dimensions for single bits in a high areal density bit patterned media (beyond 1 Tb/in^2) [28]. A straight hard/soft interphase was defined at a model thickness of 10 nm and an additional obstacle of one phase was embedded in the other phase. The influence of the obstacle size and position on H_c and the domain wall motion were studied.
2. In the second type the models have dimensions: 1 nm x 100 nm x 20 nm (Fig.31.C). Because of a significantly shorter length in x-direction (only 1 nm) this kind of models are named quasi 2D. A complex rough interphase with many irregular obstacles was generated for the switching field analysis. The nanostructures of these quasi 2D models are very similar to the real ones of the FePt thin films (please compare Fig.30 with Fig.31.C).
3. The quasi 2D models do not have a realistic dimensions of the FePt films, hence also a corresponding 3D structures were created. They belong to the third model type (Fig.31.B) and have the same dimensions as in the first type. The variation of the hard phase distribution along the thickness of the model (z direction) was investigated. This models have a fixed 4 nm thick layer of only hard phase. On top of it mixed region occur, where both, hard and soft phase exist. In the discussion this region is denoted as an interphase region.

For the type two and three the hard phase distribution in the interphase region was randomly generated by an accept-reject algorithm according to

$$\text{linear:} \quad f(z) = az + b \quad (38)$$

$$\text{logistic:} \quad f(z) = 1 - 1/[1 + \exp((a - z)/b)] \quad \text{or} \quad (39)$$

$$\text{quadratic:} \quad f(z) = a(z - b)^2 \quad (40)$$

function. The parameters a and b were suitably varied, so that for each distribution type a variable interphase thickness was studied. Quasi 2D models with 10 nm and 3D models with 9 nm, 15 nm, 18 nm and 21 nm thick interphases are presented in this thesis.

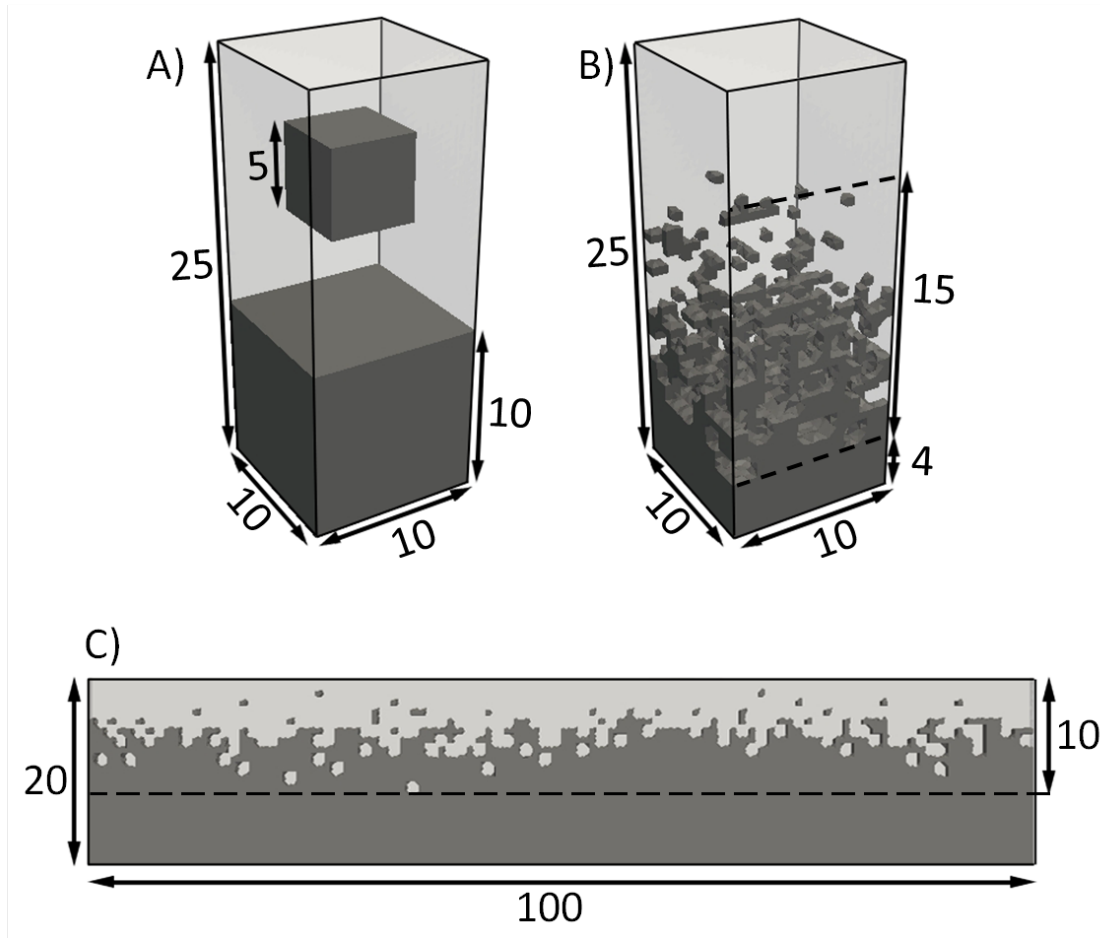


Figure 31: Visualization of the finite element models. Dark grey areas correspond to the hard phase and light grey to the soft phase. All dimensions are given in nanometers. A) A 3D model with a single obstacle with an edge length equal to 5 nm and positioned 6 nm above the flat interphase. B) A 3D model with rough, 15 nm thick interphase, where the hard phase transition follows a quadratic distribution. The bottom hard layer was fixed as 4 nm thick. C) A quasi 2D model (dimensions 1 nm x 100 nm x 20 nm) with 10 nm thick interphase and hard phase transition according to a logistic distribution.

The accept-reject algorithm uses a random number generator between 0 and 1, which is included in all standard programming languages libraries (FORTRAN, Python etc.). The generated number is compared with the value of the distribution function at a certain z value in a given column of the medium. The comparison is done at a center of each cubic discretization cell, hence in 1 nm step size in x,y,z-directions. If the random number is below the function value at a certain position, the hard phase material parameters are assigned to the given cubic and vice versa, meaning if the random number is above the function value the soft phase parameters are assigned. The part of this algorithm responsible for fitting random numbers into a given analytical function was written in FORTRAN language and saved as a program: **X_distribution.exe**, where X is one of the possible distributions: linear, logistic

or quadratic. The source code of this program can be found in the A Appendix. Assigning the material parameters to the discretization cells was done with help of **phasemaker.exe** written by J.Lee [21].

An example of the analytical functions together with the accept-reject fitting are presented for the quasi 2D models in Fig.32. The black curves are described by the following equations (with given parameters a and b):

$$\text{linear:} \quad f(z) = -0.1z + 2 \quad (41)$$

$$\text{logistic:} \quad f(z) = 1 - 1/[1 + \exp(10 - z)] \quad (42)$$

$$\text{quadratic:} \quad f(z) = 0.01(z - 20)^2 \quad (43)$$

Also the generated interphases are shown (Fig.32.A) for a better comparison between different distributions.

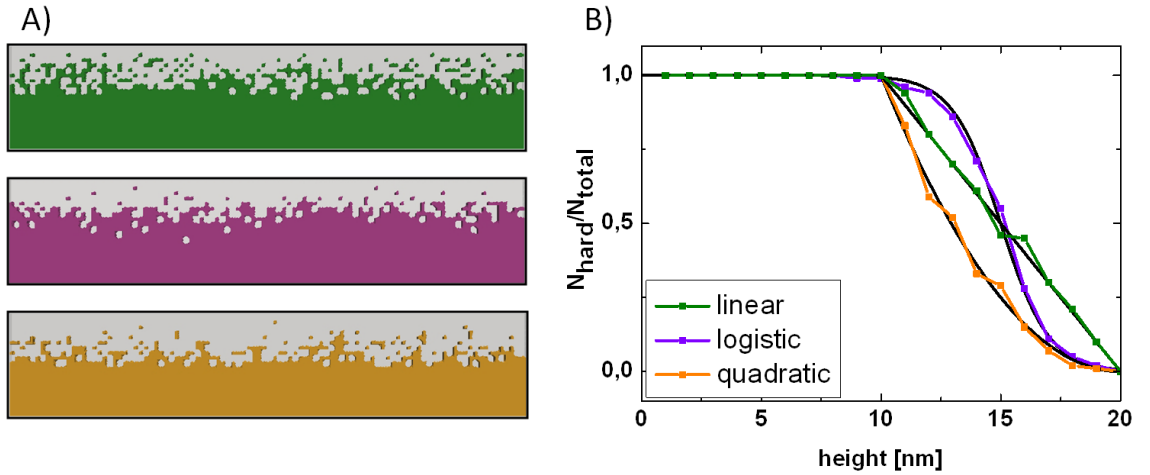


Figure 32: A) Visualisation of the models with linear (green), logistic (violet) and quadratic (yellow) distribution of the hard phase in the interphase region. B) Diagrams with the hard phase distributions. The coloured lines with points corresponds to the distributions generated by the accept-reject algorithm. The black lines denote used analytical functions.

The accept-reject algorithm allows to create models with different interphases but the same distribution of the hard/soft phase for a defined analytical function. This is visualized below in Fig.33 for 3D models. For a chosen linear function (Eq.38) with given parameters a and b the programs **accept-reject.exe** and subsequently **phasemaker.exe** were run three times. One can see that all three generated distributions are well fitted by the analytical function (Fig.33.B). The interphases of these models, however look different (Fig.33.A). In order to calculate standard deviations of the results ten 3D models were created for each distribution function.

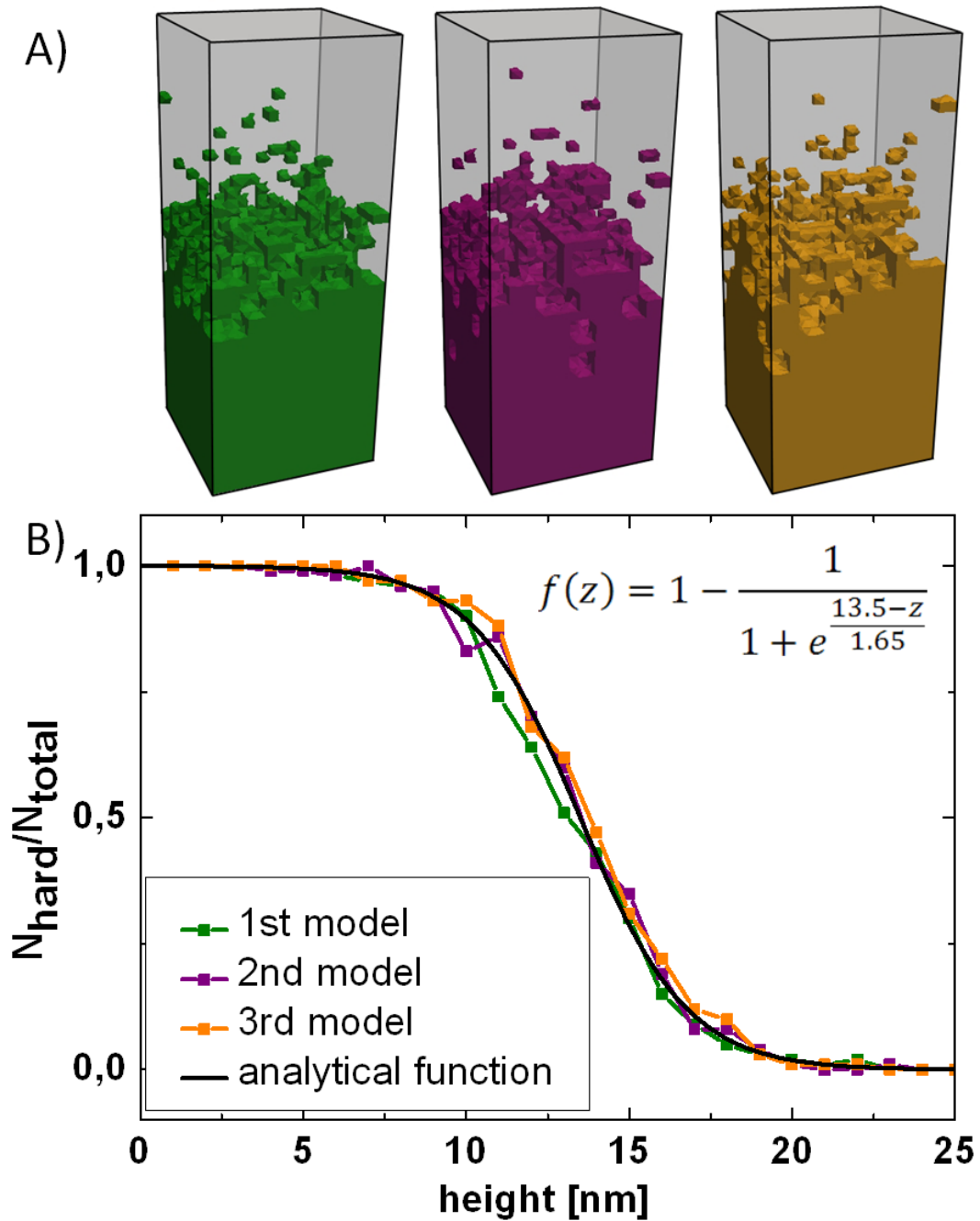


Figure 33: A) Three different models with the logistic distributions of the hard phase shown in B). The black line and the equation belong to the analytical function. The green model corresponds to the green dotted line, ect.

All the FE models were prepared in the GiD 9.3.1b software, which is a graphical user interface suitable for geometrical modelling of solids. The exchange length of such material as FePt L_{10} is equal to 1.4 nm, hence the mesh size for all models was set to smaller value equal to 0.5 nm. The output file set generated by GiD is listed in Tab.4.

Generated by GiD files together with an adequately prepared parameter file were

file extension (modelname.*)	contents
.inf	number of nodes, volume and surface elements
.knt	cartesian coordinates of all nodes
.ijb	list of surface triangles
.ijk	list of volume tetrahedrons
.ijl	list of line elements (should be empty)
.ini	initial magnetisation in each grain
.krn	material parameters of each grain
.gbe	intergranular exchange

Table 4: Output file set generated by GiD software [21].

used as an input for the finite element calculations. In the control parameter file (model.par) one defines the problem by giving the problem name, the initial and final time of the simulation. One also sets the mesh scaling factor, which in our case was 10^{-9} and other parameters, such as dynamics of the external field.

A time dependency of the magnetisation and hysteresis curves for all models were obtained from the solution of the Landau-Lifshitz equation at 0K, hence thermal activations are neglected. This, however, does not hinder a comparison of results for different models, because their properties were simulated under the same conditions. For the media similar to the one described in this paper (with $K_1(x) \sim x^2$) it has been already shown, that the stray field changes the coercive field only by a few percent [6]. Thus, demagnetization factors are not considered. Such an approach additionally simplifies the comparison between the pinning fields obtained from the simulations and analytical formula (Eq.(35)), which was derived neglecting the magnetostatic energy.

The material parameters, taken from the FePt L1₀/A1 example, are

$$K_1 = 5 \cdot 10^6 \text{ J/m}^3, \quad J_s = 1.58 \text{ T}, \quad (44)$$

for the magnetically hard phase (L1₀) and

$$K_1 = 10^5 \text{ J/m}^3, \quad J_s = 1 \text{ T}, \quad (45)$$

for the magnetically soft (A1) phase [9]. The directions of the magnetocrystalline anisotropy of both phases are parallel to the thickness of the medium (z-direction). The exchange constant within and between both phases is chosen to be $A = 10^{-11} \text{ J/m}$, which means that the two phases are strongly exchange-coupled. The simulation results written in the output files with extension .inp were analysed with help of ParaView visualisation application allowing to create three dimensional maps

of local magnetisation orientation. The hysteresis curves were plotted in Origin data analysis software.

4.3 Results and discussion

Models with a single inclusion were simulated, where the L_{10} cubic obstacle edge length (l_O) ranges from 3 nm to 6 nm. The distance from the planar interphase to the bottom surface of the cube (d_O) was varied between 0 and 6 nm in steps of 1 nm. Both dimensions (l_O and d_O) are chosen around the value of the Bloch domain wall width for the hard L_{10} phase, equal to around $d_B = 4.44$ nm.

The effect of the inclusion size and position on the switching behaviour is not strictly separable, which will be discussed in the following. Figure 34 shows the influence of the l_O value at the two extreme obstacle positions: 6 nm (Fig.34.I,III,IV) and 0 nm (Fig.34.II,V,VI).

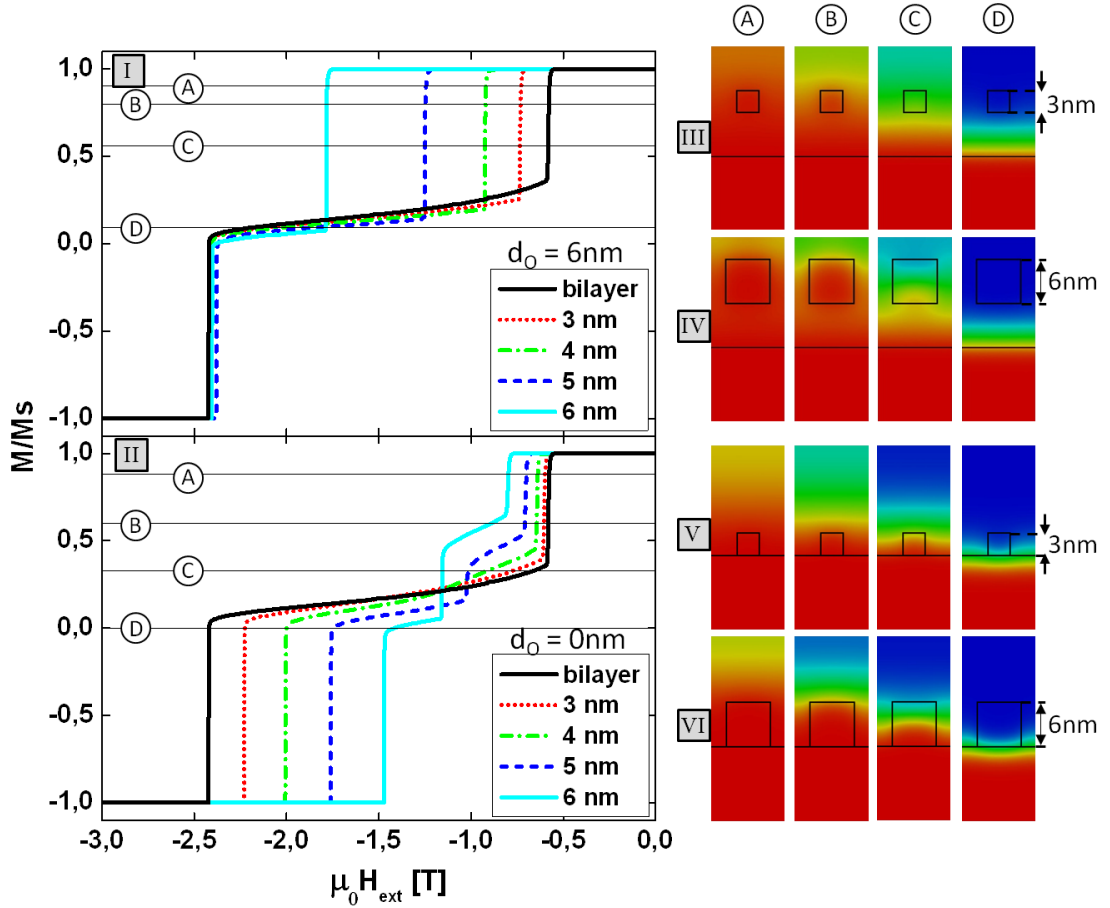


Figure 34: Left: Magnetisation curves for the models with obstacles edge length l_O varied from 3 nm to 6 nm. The inclusion was positioned: I) $d_O = 6$ nm above the flat interphase, II) directly at the flat interphase. Right: domain wall motion for selected models, where a cross section was taken in the middle of the cuboid. A,B,C,D are different states of the reversal process, as pointed out in I and II.

The two diagrams present magnetisation curves for the models with variable obstacle sizes. As a reference, the magnetisation curve for a bilayer is plotted. This bilayer has the same dimensions as the other models, but no obstacle inside.

Colourful maps in Fig.34.III,IV,V and VI represent magnetisation states at the middle cross section of the models. Red colour symbolizes magnetisation pointing up, dark blue - magnetisation pointing down. All the intermediate colours occur within the domain wall and represent local magnetisation states within up and down.

At the distance of 6 nm (Fig.34.I) the obstacle size does not change significantly the coercive field. The nucleation field (H_N), however, increases nonlinearly with l_O . This is mainly due to two reasons. Firstly, as l_O increases the pinning field (H_P) on the obstruction becomes stronger, which contributes to H_N . Secondly, the distance between the inclusion and the model top surface decreases with increasing obstacle size. This contributes to the domain wall nucleation and growth processes. For $l_O = 3$ nm the distance from the model top surface is equal to 6 nm and for $l_O = 6$ nm is equal to 3 nm. The domain wall, thus, has twice more space for growing before it gets pinned at the inclusion (Fig.34.III,IV.A,B) in the case of $l_O = 3$ nm. In both cases, however, there is still not sufficient space to fully form the domain wall in the soft phase before interacting with the obstacle. That is one reason why there is no additional third step between nucleation and coercivity field (equal to H_P at the planar interphase) in the magnetisation curves.

A further reason for this is visible in Fig.34.II, where the hysteresis curves are plotted for the obstacles touching the planar interphase. Evidently, the three-step curves occur only for $l_O = 5$ nm and $l_O = 6$ nm. This is due to the fact that the domain wall, with $d_B = 4.44$ nm in the hard phase, "sees" the obstacle, which is larger than itself, and is strongly pinned/bent on it (Fig.34.VI.B,C). When l_O is smaller than d_B , the domain wall is only slightly perturbed on the obstacle (Fig.34.V.B,C). The material properties are averaged over the domain wall width, thus a small obstacle is recognized as a gradual change of K_1 and J_s instead of a step-like change. Figure 34.II also shows, that at 0 nm distance H_c strongly decreases with the inclusion size, whereas H_N slightly increases.

The fact that larger obstacles help to switch the medium can be explained by the stiffness of the domain wall. This can be seen in Fig.35.II and III: as soon as the pinning at the obstacle is overcome, the domain wall is compressed inside the obstacle (Fig.35.II.C) and rapidly moves to the other side of it (Fig.35.II.D). This shapes the domain wall arc-like. Due to the intrinsic stiffness, the domain wall needs a certain space to straighten and decompress again. If d_O is small, the domain wall has not enough space to relax and it meets the interphase while still carrying the energy surplus gained by passing through the inclusion. This energy is used to

overcome the pinning at A1/L1₀ plane (Fig.35.II.E). If, however, d_O is sufficiently large the domain wall does relax (Fig.35.III.D) and the energy gained while passing the obstacle is lost. This means, that there is no additional energy helping to overcome the pinning at the planar interphase. From the magnetisation curves presented in Fig.35.I one can see for which values of d_O the energy transfer from the obstacle to the A1/L1₀ interphase occurs: H_c is significantly reduced if $d_O > d_B$. The coercive fields for models with $d_O = 5$ nm and $d_O = 6$ nm are equal to H_c of the bilayer with the ratio of hard/soft phase corrected by the obstacle volume (L1₀ with 11.25 nm height, not shown here). Thus, the domain wall width plays an important role in the above described processes.

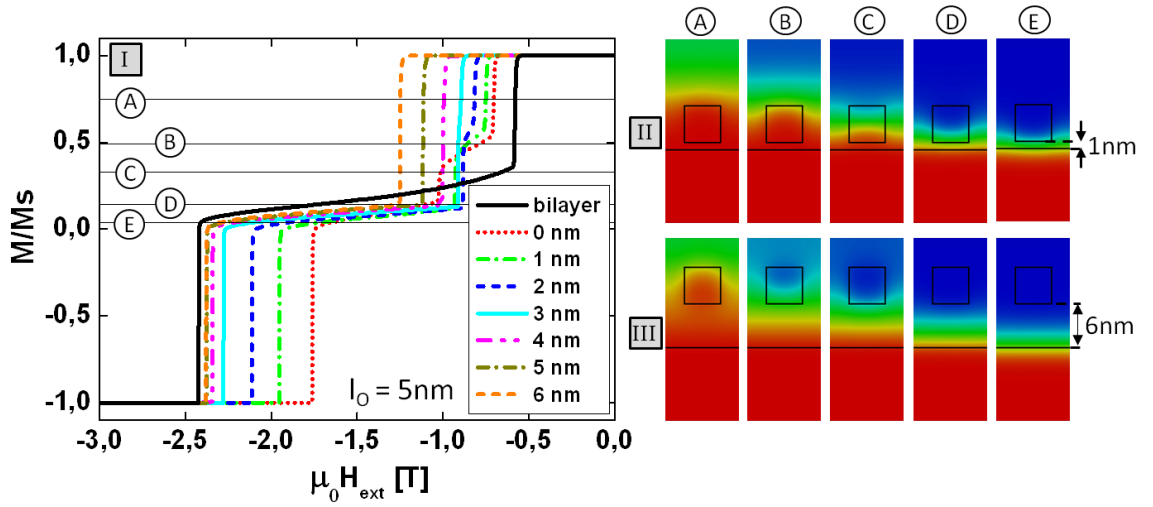


Figure 35: Simulation results for the single obstacle models. I) Magnetisation curves for obstacles with the same sizes ($l_O = 5$ nm) but variable position d_O above the flat interphase (values in the legend). II) and III) show domain wall motion for selected models, where a cross section was taken in the middle of the cuboid. A,B,C,D,E are different states of the reversal process, as pointed out in I.

Up to now only obstacles of a hard phase embedded in the soft phase were considered. Figure 36 shows however that the type of the obstacle (if it is hard or soft) does not play an important role. Two pairs of the models were here considered. In the first pair the obstacle size l_O is 4 nm, in the second 2 nm. In both cases the inclusion was positioned $d_O = 2$ nm from the flat interphase. The hard obstacle was embedded in the soft phase and the soft obstacle in the hard phase, as schematically shown in Fig.36.B. In Fig.36.A the red hysteresis curves correspond to the models which inclusions had $l_O = 2$ nm and the blue curves to the one with $l_O = 4$ nm. As one can see the switching field within one pair is very similar: for the blue pair $H_{sw} \approx 2.4$ T and for the red pair $H_{sw} \approx 2.3$ T. The difference is visible in the second decimal place and it gives the slightly higher values for the soft phase inclusions.

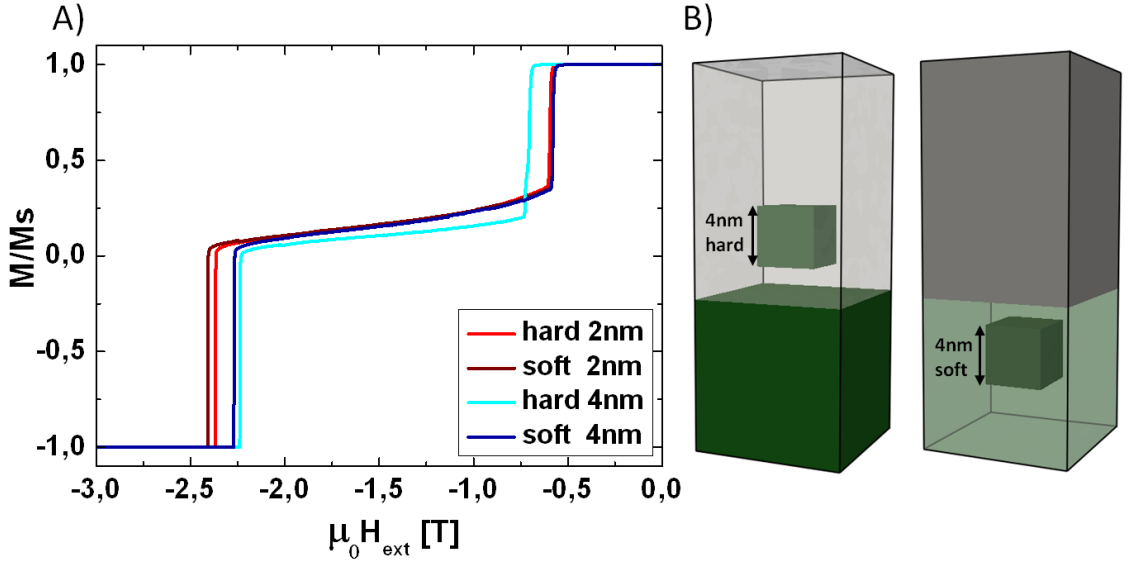


Figure 36: A) Hysteresis curves for two pairs of models. First pair, red curves, corresponds to the models with inclusion size $l_O = 2$ nm. Second pair, blue curves, corresponds to the models with $l_O = 4$ nm. In both cases the distance of the obstacle from the flat interphase was $d_O = 2$ nm. In the legend the inclusion type (hard, soft) and the l_O values are given. B) Visualization of the second model pair. The green colour denotes the hard phase, the grey - the soft phase.

So far the discussion focused on the influence of the individual obstacle size, position and type on the switching behaviour. In reality, however, the exchange spring media have more complicated structures. That is why models with complex rough interphases were generated.

The distribution functions for the quasi 2D models were already given in Eq.41,42,43 and presented in Fig.32. Simulated results for these structures are presented in Fig.37. Figure 37.I shows hysteresis curves for all three rough interphase models together with a bilayer reference curve. This bilayer has 15 nm thick hard phase and 5 nm thick soft phase, which is approximately equal to the hard/soft ratio in the rough interphase models. Despite the same hard/soft ratio, magnetisation curves differ significantly between the models. The highest H_{sw} corresponds to the bilayer, for which a significant difference between the nucleation and the maximal pinning field occur. Switching field reduced by 7% with respect to the bilayer corresponds to the linear case. Here the nucleation field is responsible for the magnetic reversal process. In logistic and quadratic case the maximal pinning field is only slightly higher than the nucleation field. The lowest H_{sw} , reduced by 36%, characterize the quadratic model. The values of H_{sw} and their relative reductions with respect to $H_{sw,bilayer}$ are given in the Tab.5.

distribution type	H_{sw} [T]	reduction of H_{sw} [%]
bilayer	2.76	
linear	2.57	7
logistic	2.04	26
quadratic	1.63	38

Table 5: The values of the switching field for all generated quasi 2D models as well as relative reductions of the switching fields with respect to H_{sw} of the bilayer.

The domain wall motions are presented in Fig.37.II. For all rough interphase models the nucleation starts at a place with the locally smallest anisotropy constant, which is positioned within upper part of the models (Fig.37.II.A). In spite of a still not completely reversed soft part the domain wall in a state B (Fig.37.II.B) starts to penetrate into the hard phase. As soon as the pinning at the interphase is overcome the domain wall goes locally to the bottom of the structure (Fig.37.II.C). Afterwards, it spreads horizontally till the whole model is reversed (Fig.37.II.D). This magnetisation dynamics is much more complicated than in the bilayer case. Here the domain wall moves almost perfectly planary from the top to the bottom (Fig.37.II bilayer).

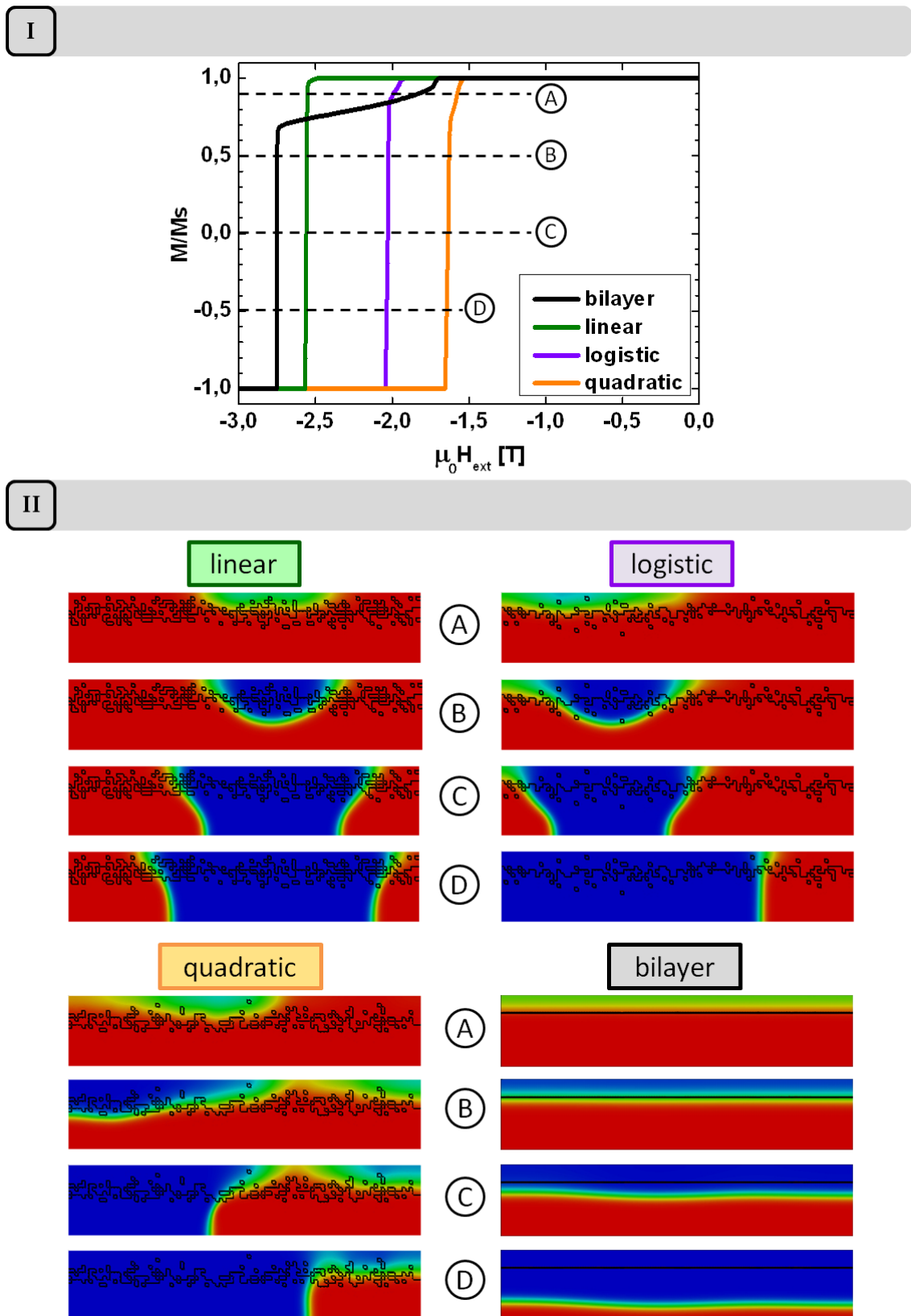


Figure 37: I) Hysteresis curves for quasi 2D models with linear (green), logistic (violet) and quadratic (yellow) distributions of the hard phase in the interphase region. For a better comparison also a curve for a bilayer (black) is plotted. II) Domain wall movement snapshots for all 4 cases. A,B,C,D correspond to the magnetisation states marked by the dashed lines in I).

The maximal switching field reduction in case of the quadratic models is not only characteristic for the quasi 2D models but also for the 3D structures. The complex domain wall dynamics is however exclusively found in the quasi 2D models. A complementary discussion of the 3D structures is presented below.

Figure 38 shows magnetisation curves for the selected 3D bits with linear, logistic and quadratic $L1_0$ distributions with interphase thicknesses (t_{int}) equal to 9,15,18 and 21 nm. The real average width of the interphase can slightly deviate from these values due to the fitting method (accept-reject algorithm). The bottom hard layer had always fixed thickness of 4 nm. As already mentioned, for each analytical function ten bits were simulated. For sake of simplicity, the hysteresis was plotted for each case only for a single bit. In Fig.38.A one can observe, that for all three types of models with $t_{int} = 9$ nm the switching field is defined by the pinning field, because $H_{P,max} > H_N$. In case of $t_{int} = 15$ nm the switching for some of the linear bits (with linear distribution) was defined by H_P (as in Fig.38.B) and for some by H_N . Similar characteristic occurs for the quadratic case at $t_{int} = 18$ nm (Fig.38.C) and for the logistic case at $t_{int} = 21$ nm (Fig.38.D).

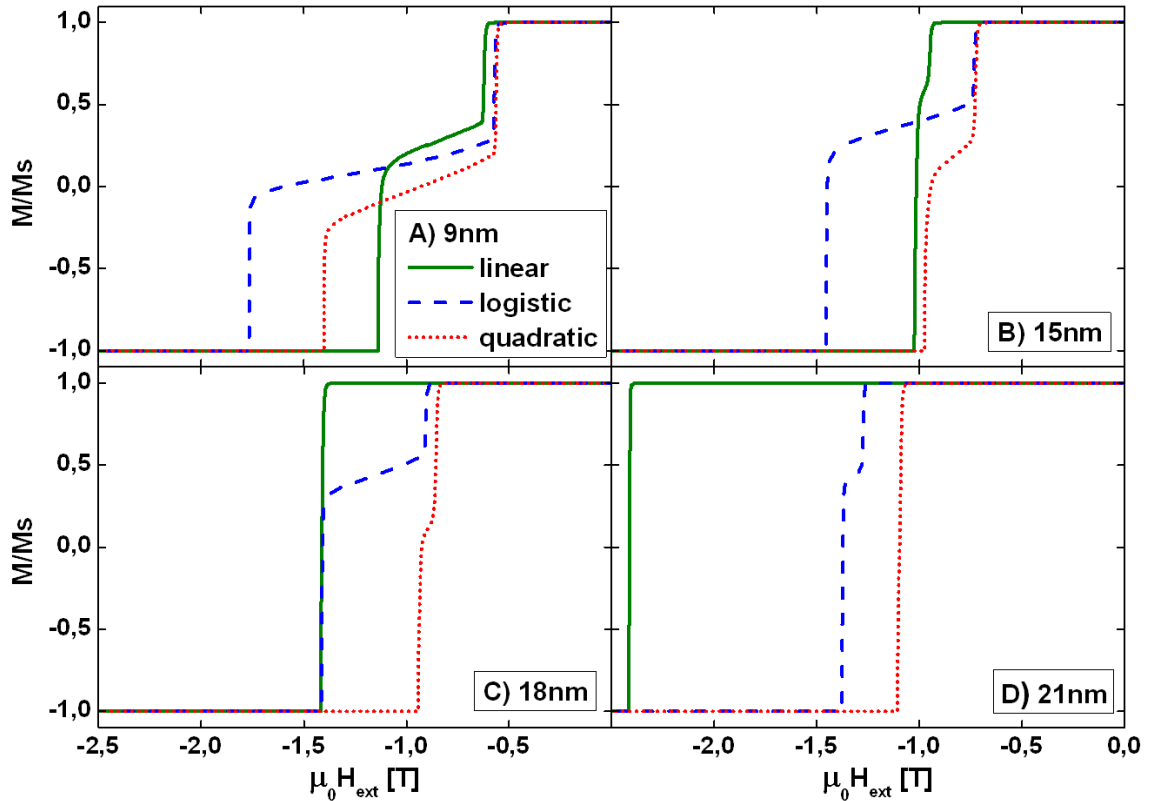


Figure 38: Magnetisation curves for the rough interphase models with the following distributions of the hard phase: linear (green, solid lines), logistic (blue, dashed lines) and quadratic (red, dotted lines). The thicknesses of the interphase were chosen to be: A) 9 nm, B) 15 nm, C) 18 nm, D) 21 nm.

For a better overview hysteresis curves for all ten quadratic bit models with $t_{int} = 18$ nm are presented in Fig.39. The standard deviation of the switching field in this case was equal to 2% and within this small value one could still recognize the curves with a step ($H_{sw} = H_{P,max}$) and without it ($H_{sw} = H_{N,max}$). We can hence approximatively say that in this case $H_{P,max} \approx H_N$ and the domain wall movement is no longer stable.

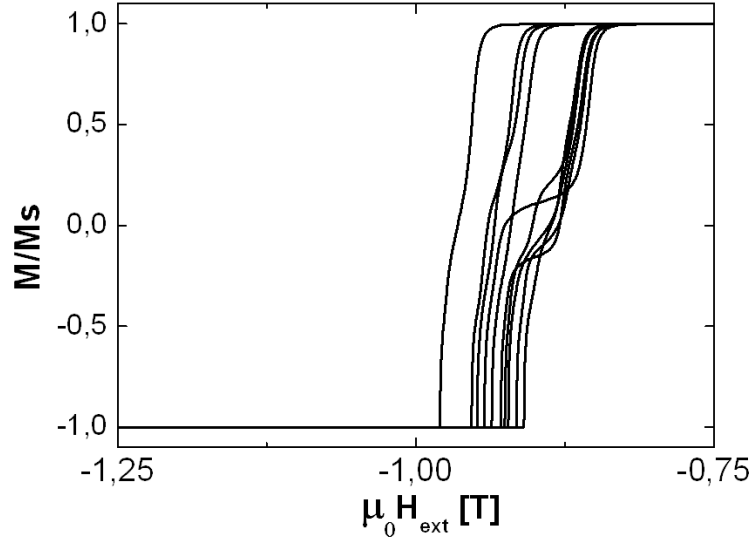


Figure 39: Hysteresis curves for ten randomly generated quadratic bit models with 18 nm thick interphase. Some of the curves have a characteristic step, some not. For the one with the step the switching field is defined by the maximal pinning field, for the rest by the nucleation field.

For the still stable domain wall movement mechanism examples are presented in Fig.40. In both logistic models, with $t_{int} = 9$ nm (Fig.40.I) and with $t_{int} = 18$ nm (Fig.40.II), the domain wall first nucleates in the soft part of the bit. Afterwards, it arrives at the interphase, where it is pinned and gradually compressed. In this case the domain wall width (d_{wall}) can be described by the following equation [29],

$$d_{wall} = \pi \sqrt{\frac{A}{H_{ext} J_S + K_1(z)}}, \quad (46)$$

which shows that the compression occurs due to increasing external field (H_{ext}) as well as anisotropy constant ($K_1(z)$).

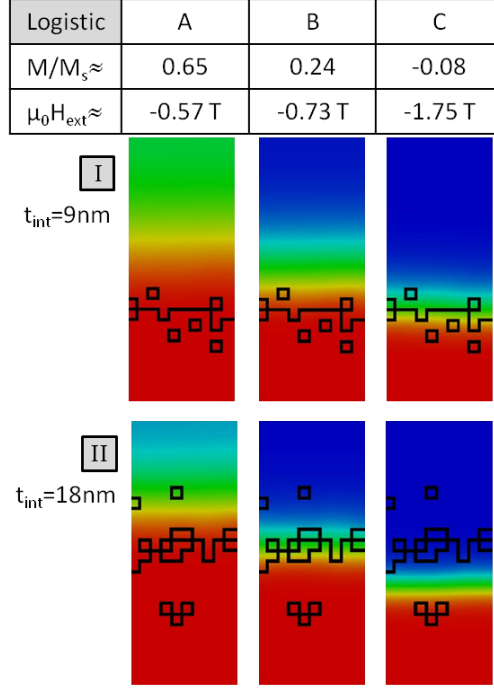


Figure 40: An example of the domain wall movement for the bits with the logistic distribution of the hard phase and the interphase roughness equal to: I) 9 nm and II) 18 nm. The images show cross sections in the middle of the cuboid. Black lines mark the interphases. The external field strength and net magnetisation value, at which the snapshots were taken, are given in the table.

Despite the irregular interphase, marked in the figures by black lines, the domain wall stays planar with only small perturbations. This means, that the material parameters, such as K_1, J_S and A , can be averaged over the values in xy -planes and their dependency on z -coordinate looks as following,

$$\begin{aligned}
 J_S(z) &= J_{\text{hard}} \cdot f(z) + J_{\text{soft}} \cdot (1 - f(z)) \\
 K_1(z) &= K_{\text{hard}} \cdot f(z) + K_{\text{soft}} \cdot (1 - f(z)),
 \end{aligned} \tag{47}$$

where $f(z)$ is a chosen distribution function and hard/soft material parameters are the corresponding one of the L_{10}/A_1 phase (Eq.(44) and (45) respectively).

Equations (47), (45), (44) and (35) were used to obtain the switching fields for different distributions. Analytically calculated values were compared with numerical simulation results and presented in Fig.41. The best agreement occurs for the quadratic case. Here the largest discrepancy in the coercive field (~ 0.38 T) occurs at $t_{\text{int}} = 21$ nm. However, at this point the switching is no longer characterized by the pinning field but rather by the nucleation field, as it was shown in Fig.38.D. This is also valid for the linear case: the switching field at $t_{\text{int}} = 18$ nm and $t_{\text{int}} = 21$ nm is equal to the nucleation field.

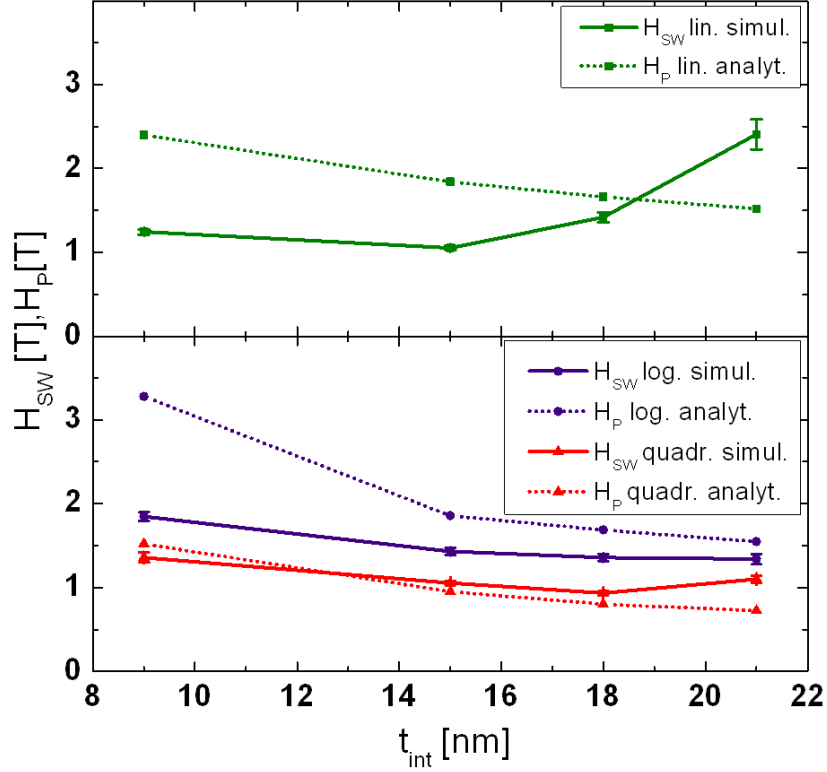


Figure 41: Switching field values for all simulated rough interphase models with 9,15,18 and 21 nm thick interphase and corresponding pinning field values calculated from the analytical formula derived in this paper.

Moreover, for thinner interphases the results from the simulations and analytical formula agree less with each other. This is due to the fact, that the theoretical approximation is only accurate when K_1 and J_S do not change rapidly in the interphase region. Since the variation of material parameters is described by a given distribution $f(z)$, this means that better analytical/simulation agreement occurs for flatter functions, which also denotes thicker interphases. If the interphase thickness is comparable to the domain wall width (d_{wall}), then the material properties in the total interphase region are averaged instead of being regarded as gradually changing according to the given distribution. As it is visible in Fig.40.I.C for logistic case, the domain wall has a comparable width as the interphase. That is the reason why we observe a high discrepancy in the analytical/simulation values ($\sim 1.43T$) at $t_{int} = 9$ nm.

Finally, micromagnetic simulations show that the maximal reduction of the switching field occurs when $H_{P,max} \approx H_N$, this corresponds to the minima in the simulation curves (solid lines) in Fig.41. Similar characteristics was already described by Skomski et al. [30]. Comparing results for different distribution functions it is visible, that the smallest value of the switching field was obtained for the quadratic case at $t_{int} = 18$ nm.

5 Summary

This work was divided into two parts. Firstly, a detailed structural analysis of the FePt L1₀/A1 media was done by means of an electron microscopy. Secondly, experimentally discovered nanostructures were transferred into the Finite Element Micromagnetic models for the study of the magnetic switching mechanisms.

In the experimental part, a chemical composition of the films was proven to be 50% of Fe and 50% of Pt. Moreover, a complex granular structure of the films was observed. Finally, high resolution images revealed, that the phase distribution along the thickness of the medium is different than expected [7]: no intermediate phase between L1₀ and A1 was found, but a very rough interphase between those two phases was discovered. Such structures as obstacles of a one phase embedded in the second phase were found.

In the theoretical part it was proven by simulations, that above mentioned obstacles can reduce a switching field of the material. The inclusions, however, have to be larger than the domain wall width in the hard phase. Also the distance between the hard phase elements (eg. obstacle and flat interphase) must be smaller than the domain wall width in this phase. In such situation a transfer of the energy surplus gained during overcoming the pinning at one object (obstacle) is conserved and used to reverse the second object (flat interphase). Moreover, a variation of the hard phase distribution along the thickness of the media was studied. For all cases; linear, logistic and quadratic the minimal switching field was obtained when the values of the maximal pinning and nucleation field were equal. It was also shown that the quadratic distribution is characterized by the maximal reduction of the switching field.

Additionally, the analytical formula of the pinning field for the exchange spring media was derived. The switching field values estimated from the analytical and numerical approach are consistent as long as the nucleation field is smaller than pinning field and the interphase is thicker than the domain wall width.

In this work only magnetic behaviour within a single grain was analysed. This analysis could be broadened up by a study of an interaction between grains, which would require also a stray field consideration. Moreover, a simulation of a read/write processes for a fully formulated FePt bit patterned media would allow to investigate such properties like switching field distribution of a realistic structure.

Although the numerical study was based on the experimental TEM results obtained for FePt films, the above specified conclusions are true for any system composed of magnetically hard and soft phase. A variable distribution of the hard phase along the thickness of the medium can be obtained by changing the film fabrication conditions. For such materials as FePt L₁₀/A1 [24] or CoPt L₁₀/A1 [31], this can be done by varying the deposition temperature in the sputtering system. For films consisting of two different composites, for instance FePt (L₁₀,hard) and FeAu (L₁₀,soft) [32], the hard phase distribution could be varied by controlling the content of softer material while deposition at constant temperature.

A Appendix

Below the source code of the program: linear_distribution.exe is presented. For the logistic and quadratic case only the analytical function is changed accordingly. The output file of this program has a list of numbers of the grains which are in magnetically hard phase. This set of numbers is subsequently used as an input for the program phasemaker.exe written by J.Lee[21].

```
Program Linear_distribution
implicit none

double precision a,b,random,linear,hard,graded
integer i,j,k,ly,lx,lz

open(50,file='linear_parameters.txt') → An input file with the
read(50,*) a,b,lx,ly,lz,hard,graded linear function parameters

open (100,file='hard_grains_nr.dat') → An output file with set of
open (200,file='linear_check.dat') → An output file used by
program linear_check3D.exe

write(100,*) 'Parameter m',a
write(100,*) 'Parameter b',b
write(100,*) 'Dimention of the model Lx,Ly,Lz:',lx,ly,lz
write(100,*) 'Thickness of the hard phase',hard
write(100,*) 'Thickness of the graded phase',graded
write(100,*) 'The following grain numbers correspond to hard phase:'

write(200,*) lx,ly,lz

call init_random_seed()

do k=1,lz
  do i=1,lx
    do j=1,ly
      call random_number(random)

      if(random.lt.linear(j,a,b,hard,graded)) then
        write(100,'(I4,a1)',advance='no') ly*lx*(k-1)+lx*(j-1)+i,' '
        write(200,'(I6)',advance='no') ly*lx*(k-1)+lx*(j-1)+i
      else
        write(200,'(I6)',advance='no') 0
      end if

    end do
    write(100,*)
    write(200,*)
  end do
end do

close(100)
end program
```

!!!!!!!!! Linear function definition

```
double precision function linear(j,a,b,hard,graded)
implicit none
double precision a,b,hard,graded
integer j

if (dble(j) .le. hard) then
  linear=1.0
else
if (dble(j) .ge. (graded+hard)) then
  linear=0.0
else
  linear=a*dble(j)+b
end if
end if

end function
```

!!!!!!!!! Initialisation of the random number seed

```
SUBROUTINE init_random_seed()
  INTEGER :: i, n, clock
  INTEGER, DIMENSION(:), ALLOCATABLE :: seed

  CALL RANDOM_SEED(size = n)
  ALLOCATE(seed(n))

  CALL SYSTEM_CLOCK(COUNT=clock)

  seed = clock + 37 * (/ (i - 1, i = 1, n) /)
  CALL RANDOM_SEED(PUT = seed)

  DEALLOCATE(seed)
END SUBROUTINE
```

The following program linear_check3D.exe allows to draw the numerically obtained distributions by such software as Excel or OriginPro. It uses as an input file the output file from the program linear_distribution.exe.

```
Program linear_check3D
  implicit none
  double precision, allocatable :: F(:, :)
  integer i, j, k, l, lx, ly, lz
  integer, allocatable :: r(:, :)

  open (200, file='linear_check.dat', status='old')
  open (300, file='linear_diagram.dat')
  read(200, *) lx, ly, lz
  allocate (F(ly, lz), r(lx*lz+1, ly))

  F(:, :) = 0.0
  r(:, :) = 0.0

  do i = 2, lx*lz+1
    read(200, *) (r(i, j), j = 1, ly)
  end do

  k = 1
  do i = 2, lx*lz+1
    do j = 1, ly
      if (r(i, j).ne.0) then
        if (r(i, j).gt.(lx*ly*k)) then
          k = k + 1
        end if
        F(j, k) = F(j, k) + 1.0
      end if
    end do
  end do

  F(:, :) = F(:, :) / dble(lx)

  do j = 1, ly
    write(300, *) j, (F(j, k), k = 1, lz)
  end do

end Program
```

References

- [1] R. H. Victora and X. Shen. Composite media for perpendicular magnetic recording. *IEEE Transactions on Magnetics*, 41(2):537– 542, February 2005.
- [2] D. Suess, T. Schrefl, R. Dittrich, M. Kirschner, F. Dorfbauer, G. Hrkac, and J. Fidler. Exchange spring recording media for areal densities up to 10 Tbit/in². *Journal of Magnetism and Magnetic Materials*, 290-291(0):551–554, April 2005.
- [3] J.-P. Wang, W. Shen, and J. Bai. Exchange coupled composite media for perpendicular magnetic recording. *IEEE Transactions on Magnetics*, 41(10):3181– 3186, October 2005.
- [4] D. Suess, T. Schrefl, S. Fahler, M. Kirschner, G. Hrkac, F. Dorfbauer, and J. Fidler. Exchange spring media for perpendicular recording. *Applied Physics Letters*, 87(1):012504–012504–3, July 2005.
- [5] F. Garcia-Sanchez, O. Chubykalo-Fesenko, O. Mryasov, R. W. Chantrell, and K. Yu. Guslienko. Exchange spring structures and coercivity reduction in FePt/FeRh bilayers: A comparison of multiscale and micromagnetic calculations. *Applied Physics Letters*, 87(12):122501, September 2005.
- [6] D. Suess. Multilayer exchange spring media for magnetic recording. *Applied Physics Letters*, 89(11):113105, September 2006.
- [7] V. Alexandrakis, Th. Speliotis, E. Manios, D. Niarchos, J. Fidler, J. Lee, and G. Varvaro. Hard/graded exchange spring composite media based on FePt. *Journal of Applied Physics*, 109(7):07B729, March 2011.
- [8] Y. Misumi, S. Masatsuji, R. Sahara, S. Ishii, and K. Ohno. A lattice monte carlo simulation of the FePt alloy using a first-principles renormalized four-body interaction. *The Journal of Chemical Physics*, 128(23):234702, June 2008.
- [9] J. Lee, V. Alexandrakis, M. Fuger, B. Dymerska, D. Suess, D. Niarchos, and J. Fidler. FePt L10/A1 graded media with a rough interphase boundary. *Applied Physics Letters*, 98(22):222501, May 2011.
- [10] S. Chikazumi and Ch. D. Graham. *Physics of Ferromagnetism*. Clarendon Press, April 1997.
- [11] A. Aharoni. *Introduction to the Theory of Ferromagnetism*. Oxford University Press, 2000.
- [12] G. Hilscher. Festkoerperphysik I, Teil 2, Magnetismus und Supraleitung. Vienna University of Technology, Solid State Insitute, 2010.

-
- [13] H. Kronmüller and M. Faehle. *Micromagnetism and the Microstructure of Ferromagnetic Solids*. Cambridge University Press, August 2003.
- [14] D. Suess, J. Lee, J. Fidler, and T. Schrefl. Exchange-coupled perpendicular media. *Journal of Magnetism and Magnetic Materials*, 321(6):545–554, March 2009.
- [15] T. B. Massalski, J. L. Murray, L. H. Bennett, and H. Baker. *Binary alloy phase diagrams*. American Society for Metals, 1986.
- [16] Y. Ding, S.A. Majetich, J. Kim, K. Barmak, H. Rollins, and P. Sides. Sintering prevention and phase transformation of FePt nanoparticles. *Journal of Magnetism and Magnetic Materials*, 284(0):336–341, December 2004.
- [17] J. F. W. Bowles. Platinum-iron alloys, their structural and magnetic characteristics in relation to hydrothermal and low-temperature genesis. *Mineralogy and Petrology*, 43(1):37–47, 1990.
- [18] T. Burkert, O. Eriksson, S. Simak, A. Ruban, B. Sanyal, L. Nordstroem, and J. Wills. Magnetic anisotropy of L1₀ FePt and Fe_{1-x}Mn_xPt. *Physical Review B*, 71(13), April 2005.
- [19] Ch. Brombacher. *Rapid thermal annealing of FePt and FePt/Cu thin films*. PhD thesis, Chemnitz University of Technology, September 2010.
- [20] J.M. Zuo and J.C. Mabon. Web-based electron microscopy application software: Web-emaps. *Microsc Microanal* 10(Suppl 2), <http://emaps.mrl.uiuc.edu/>, 2004.
- [21] J. Lee. *Inhomogenous magnetization processes in advanced recording media*. Dissertation, May 2011.
- [22] D. Suess. *Micromagnetic Simulations of Antiferro- and Ferromagnetic Structures for Magnetic Recording*. Vienna University of Technology, June 2002.
- [23] T. Shima, K. Takanashi, Y. K Takahashi, and K. Hono. Preparation and magnetic properties of highly coercive FePt films. *Applied Physics Letters*, 81(6):1050–1052, August 2002.
- [24] J. Lee, B. Dymerska, J. Fidler, V. Alexandrakis, Th. Speliotis, D. Niarchos, P. Pongratz, and D. Suess. Fabrication and high resolution electron microscopy study of FePt L1₀/A1 graded exchange spring media. *In review*, 2012.
- [25] F. Stevie, C. Vartuli, L. Giannuzzi, T. Shofner, S. Brown, B. Rossie, F. Hillion, R. Mills, M. Antonell, R. Irwin, and B. Purcell. Application of focused ion

- beam lift-out specimen preparation to tem, sem, stem, aes and sims analysis. *Surface and Interface Analysis*, 31(5):345–351, January 2001.
- [26] B. Dymerska. Investigation of the nanoporated zro₂ membrane and fe-co ultrafine particles with tem. Vienna University of Technology, Solid State Institute, January 2010.
- [27] S. Okamoto, N. Kikuchi, O. Kitakami, T. Miyazaki, Y. Shimada, and K. Fukamichi. Chemical-order-dependent magnetic anisotropy and exchange stiffness constant of fept (001) epitaxial films. *Phys. Rev. B*, 66:024413, July 2002.
- [28] A. Cattoni, J. Chen, and D. Decanini. *Recent Advances in Nanofabrication Techniques and Applications*. Number ISBN 978-953-307-602-7. InTech, December 2011.
- [29] S. Mukherjee and L. Berger. Switching of composite media by wall propagation. *Journal of Applied Physics*, 99(8):08Q909–08Q909–3, April 2006.
- [30] R. Skomski, T. A George, and D. J Sellmyer. Nucleation and wall motion in graded media. *Journal of Applied Physics*, 103(7):07F531–07F531–3, March 2008.
- [31] J. A Christodoulides, Y. Huang, Y. Zhang, G. C Hadjipanayis, I. Panagiotopoulos, and D. Niarchos. CoPt and FePt thin films for high density recording media. *Journal of Applied Physics*, 87(9):6938–6940, May 2000.
- [32] F. Wang, X. Xu, Y. Liang, J. Zhang, and H. Wu. FeAu/FePt exchange-spring media fabricated by magnetron sputtering and postannealing. *Applied Physics Letters*, 95(2):022516–022516–3, July 2009.

Curriculum Vitae

Personal Information

Name: Barbara Dymerska
Date of birth: 04/12/1988
Place of birth: Gdansk
Nationality: Polish
Phone: 0 6641739080
E-mail: barbara.dymerska@gmail.com
Address: Goldeggasse 20/2, 1040 Wien

Education

From 10/2011 Master program in Technical Physics,
Vienna University of Technology
10/2011 Bachelor degree in Technical Physics,
Vienna University of Technology
From 02/2011 Master program in Technical Physics, Nanotechnology,
Gdańsk University of Technology
02/2011 Bachelor degree in Technical Physics, Nanotechnology,
Gdańsk University of Technology
From 10/2011 Bachelor program in Technical Physics,
Vienna University of Technology
10/2009-06/2010 ERASMUS exchange student at
Vienna University of Technology
10/2007-01/2011 Bachelor program in Technical Physics, Nanotechnology,
Gdańsk University of Technology
05/2007 Matura (school leaving examination), Gdańsk

List of publications

1. B. Dymerska, J. Lee, J. Fidler, D. Suess, *Micromagnetic study of exchange spring media with a rough interphase on example of FePt films*, J. Phys. D (2012), in review
2. J. Lee, B. Dymerska, J. Fidler, V. Alexandrakis, T. Speliotis, D. Niarchos, P. Pongratz, D. Suess, *Fabrication and High resolution electron microscopy study of FePt L1₀/A1 graded exchange spring media*, Nanotechnology (2012), in review
3. S. Thomas, G. Pookat, S. Nair, M. Daniel, B. Dymerska, A. Liebig, S. Al-Harthi, R. Ramanujan, M. Anantharaman, J. Fidler and M. Albrecht, *Exchange bias effect in partially oxidized amorphous Fe-Ni-B based metallic glass nanostructures*, J. Phys.: Condens. Matter (2012), in printing
4. J. Lee, Ch. Brombacher, J. Fidler, B. Dymerska, D. Suess, M. Albrecht, *Contribution of the easy axis orientation, anisotropy distribution and dot size on the switching field distribution of bit patterned media*, Appl. Phys. Lett. 99, 062505 (2011)
5. J. Lee, V. Alexandrakis, M. Fuger, B. Dymerska, D. Suess, D. Niarchos, J. Fidler, *FePt L1₀/A1 graded media with a rough interphase boundary*, Appl. Phys. Lett. 98, 222501 (2011), DOI:10.1063/1.3595307
6. B. Dymerska, S. Traxler, *Investigation of the ECG signal dependent on lung volume, pressure and breathing resistance for the improvement of sleep apnea diagnosis*, May 2010 Gdańsk, Poland, Proceedings of the 13th International Symposium of Students and Young Mechanical Engineers, ISBN 978-83-88579-42-4
7. B. Dymerska, *Emergency-evacuation system for hospitals*, May 2009 Gdańsk, Poland, Proceedings of the 12th International Symposium of Students and Young Mechanical Engineers, ISBN 978-83-88579-17-2
8. W. Sadowski, B. Dymerska, *Study of thermal stability of Nd_{2-x}Ce_xCuO_{4-y} single crystals in a reducing atmosphere*, March 2009 Vienna, Austria, Proceedings of the Viennano'09, ISBN 978-3-90165733-7

List of presentations

1. J. Fidler, J. Lee, B. Dymerska, D. Suess, *Optimization of FePt films for recording applications by micromagnetic modeling*, 25-30 March 2012, 76th Annual Meeting of the DPG and DPG Spring Meeting, Berlin, Germany.
2. B. Dymerska, J. Lee, V. Aleksandrakis, D. Niarchos, D. Suess, J. Fidler, *TEM studies and micromagnetic simulations of FePt L₁₀/A1 phase graded media*, 30 Oct.-3 Nov. 2011, 56th MMM Conference, Scottsdale, USA.
3. J. Lee, V. Aleksandrakis, B. Dymerska, M. Fuger, D. Suess, D. Niarchos, J. Fidler, *Micromagnetic simulations on FePt L₁₀/A1 phase graded media*, 25-29 April 2011, INTERMAG, Taipei, Taiwan.
4. J. Lee, D. Makarov, C. Brombacher, B. Dymerska, M. Fuger, D. Suess, M. Albrecht and J. Fidler, *TEM Studies on RTA treated FePt-based Exchange Coupled Composite Media*, 14-18 Nov. 2010, 55th MMM Conference, Atlanta, USA.
5. B. Dymerska, C. Tomastik, C. Lenauer, M. Jech, H. Störi, *Chemical surface analysis of cylinder liners affected by selected combustion products from ethanol bio-fuel*, 07-10 Sept., 37th Leeds-Lyon Symposium on Tribology, Leeds, United Kingdom.
6. J. Lee, D. Makarov, B. Dymerska, C. Brombacher, J. Fidler, M. Fuger, D. Suess and M. Albrecht, *TEM study of interface properties of FePtCu-based exchange coupled composite media*, 23-28 Aug., Joint European Magnetic Symposia, Kraków, Poland.
7. B. Dymerska, J. Lee, J. Fidler, *Investigation of the nanoporated ZrO₂ membrane and Fe-Co ultrafine particles with TEM*, 17-23 Aug., International Conference of Physics Students, Graz, Austria
8. B. Dymerska, S. Traxler, *Investigation of the ECG signal dependent on lung volume, pressure and breathing resistance for the improvement of sleep apnea diagnosis*, 20-22 May, 13th International Symposium of Students and Young Mechanical Engineers, Gdańsk, Poland
9. B. Dymerska, *Emergency-evacuation system for hospitals*, 21-23 May, 12th International Symposium of Students and Young Mechanical Engineers, Gdańsk, Poland
10. W. Sadowski, B. Dymerska, *Study of thermal stability of Nd_{2-x}Ce_xCuO_{4-y} single crystals in a reducing atmosphere*, Viennano'09, Vienna, Austria
11. B. Dymerska, *Forces dissociating molecular bonds. Magnetic biosensors.*, 20-25 April, 5th Symposium on Bio-molecular and Medical Physics, Kraków, Poland
12. B. Dymerska, *Bioethics in modern society. The light and the shadow in medicine.*, 04-12 Sept., The 54th Interational Student Conference, Tokio, Japan
13. B. Dymerska, *New application of biosensors*, 06-13 Sept., XXIII International Conference for Physics Students, Kraków, Poland

Acknowledgements

This thesis has been realised at the Solid State Institute of the Technical University of Vienna and has been supported by the European Commission via TERAMAGSTOR project on high areal density recording (No. FP7-ITC-2007-2-224001).

Firstly, I would like to thank my supervisor, Josef Fidler for giving me opportunity to work on an interesting topic in a friendly and inspiring environment. Thank you for constructive criticism and encouragements to contribute with our work to conferences and publications. I also address my acknowledgements for organising financial support for this thesis.

Secondly, I thank Jehyun Lee for introducing me to the world of transmission electron microscopy and magnetism. I appreciate your patience and time, which you have devoted to me for clear explanations. Your guidance have helped me to overcome many scientific problems.

Next, I would like to thank Dieter Suess for fruitful discussions, which have broadened my knowledge and allowed me to extend the theoretical discussion of exchange spring media by derivation of the pinning field. Thank you also for a guidance through the MMM conference.

Many thanks to Markus Fuger for helping with any software related problem as well as sharing the knowledge about micromagnetism.

I also thank Vasilis Alexandrakis and Dimitris Niarchos for providing the specimens and valuable discussions during TERAMAGSTOR meeting in Rome.

I further appreciate University Service for Transmission Electron Microscopy (USTEM) for providing investigation facilities. I show gratitude to Johannes Bernardi and Michael Stöger-Pollach for an introductory course of TEM. I thank Jakob Gruber for help during sample preparation procedures. I thank also Andreas Steiger-Thirsfeld for SEM analysis of the specimens.

I am grateful to Prof. Peter Pongratz for the discussion concerning High Resolution TEM image analysis.

Prof. Wojciech Sadowski, I thank you for the great idea to participate in Viennano'09 conference and start ERASMUS exchange in Vienna. This was a begin of a new, challenging and very interesting period of my life. Thank you also for keeping contact during this last few years and for always good advises.

Kochani rodzice, Wam będę dziękować przez całe moje życie. Mam nadzieję, że moje decyzje i osiągnięcia przynioszą Wam wiele radości.

Drogi Joni, stwierdziłam, że utrwale jednak moją wdzięczność dla Ciebie na papierze: za szczerłość i oddanie, za cierpliwość i profesjonalizm, za te ceglane filary które zbudowałeś żeby podtrzymać moją kapliczkę z zapalek.